Sci

MDPI

Article

From Ancient Aqueducts to Modern Turbines: Exploring the Impact of Nazca-Inspired Spiral Geometry on Gravitational Vortex Turbine Efficiency

Juliana Carvajal Guerra [1], Ainhoa Rubio-Clemente [1,2] and Edwin Chica [1,*]

[1] Grupo de Energía Alternativa, Facultad de Ingeniería, Universidad de Antioquia, Calle 70 No. 52-21, Medellín 050010, Colombia; juliana.carvajalg@udea.edu.co (J.C.G.); ainhoa.rubioc@udea.edu.co (A.R.-C.)
[2] Escuela Ambiental, Facultad de Ingeniería, Universidad de Antioquia, Calle 70 No. 52-21, Medellín 050010, Colombia
* Correspondence: edwin.chica@udea.edu.co; Tel.: +57-604-219-5550

Abstract

This study investigates an inlet design for a gravitational vortex turbine (GVT), drawing inspiration from the ancient Nazca puquios. The puquios are ingenious subterranean aqueducts constructed by the Nazca culture (c. 100 BC–800 AD) in southern Peru, featuring spiral ojos de agua (water eyes) used to access groundwater and stabilize flow.The primary objective was to enhance vortex stability and overall GVT efficiency under low-head, low-flow operating conditions. A parametric Nazca-type inlet feeding a conical basin was defined by two controlling factors: the number of turns (N) and the inclination angle (θ). The optimal geometry was determined through a 3^2 full factorial design, computational fluid dynamics (CFD) simulations, and response surface methodology (RSM), with vortex circulation (Γ) serving as the optimization metric. The best-performing inlet configuration ($N = 4$, $\theta = 13°$) yielded $\Gamma = 1.3459$ m^2/s. This circulation level is comparable to that reported for optimized conventional wrap-around inlets at similar flow rates, but uniquely produced a broader and more symmetric vortex structure. Subsequently, two four-bladed runners (one with twisted blades and one with curved cross-flow blades) were evaluated numerically and experimentally using a laboratory-scale prototype operated at a consistent flow rate ($Q \approx 0.00143$ m^3/s). CFD predicted maximum efficiencies of 15.37% and 17.07% for the twisted and curved runners, respectively, while experimental tests achieved 8.70% and 11.61%, demonstrating similar efficiency (η) versus angular velocity (ω) characteristics. These results indicate reduced hydraulic effectiveness of the Nazca-inspired geometry for the GVT, with experimental efficiencies below those reported in the literature.

Keywords: gravitational vortex turbine; Nazca puquios; CFD; response surface methodology; renewable energy; optimization

Check for updates

Academic Editor: Dong-Sheng Jeng

Received: 15 December 2025
Revised: 23 January 2026
Accepted: 2 February 2026
Published: 5 February 2026

Copyright: © 2026 by the authors. Licensee MDPI, Basel, Switzerland. This article is an open access article distributed under the terms and conditions of the Creative Commons Attribution (CC BY) license.

1. Introduction

The global energy crisis, driven by the recovery from the COVID-19 pandemic, rising geopolitical tensions, and persistent climate challenges, highlights the urgent need to critically reassess dependence on fossil fuels. These energy sources, primarily coal, oil, and natural gas, are the main contributors to greenhouse gas emissions, particularly carbon dioxide (CO_2), which is a central driver of global warming and climate change [1]. From a technical perspective, the combustion of fossil fuels not only releases CO_2 but also emits other pollutants that degrade air quality and pose serious health risks [2–4]. As a result,

transitioning to renewable energy sources is essential to mitigate environmental harm, reduce greenhouse gas emissions, and strengthen both energy security and resilience in the face of climate variability [5].

Among the available renewable options, hydropower represents a technically robust solution due to its capacity to generate substantial amounts of electricity with minimal direct emissions. Its ability to provide stable, dispatchable power and respond quickly to fluctuations in demand makes it a vital component of electricity grids that increasingly rely on variable sources such as wind and solar [6–8]. Large hydropower plants, in particular, can perform critical grid functions including load balancing, frequency regulation, and peak-power provision.

Nevertheless, the development of large-scale hydropower projects involves considerable environmental and socio-economic trade-offs. The construction of major dams can significantly alter river flow regimes, disrupt sediment transport processes, and degrade water quality. These changes may result in habitat loss for aquatic and terrestrial species and adverse effects on downstream ecosystems. Furthermore, large dam projects often lead to the displacement of local communities, raising complex social and ethical issues that require careful and inclusive consideration. Achieving sustainable hydropower development therefore depends on balancing technical advantages with potential environmental and social impacts [9].

In response to these limitations, low-head, run-of-the-river technologies have emerged as promising, more sustainable alternatives. Unlike conventional dam-based systems, these technologies operate without the need for large reservoirs, which significantly reduces flooding risks, sedimentation issues, and ecological disruption. Additionally, they often entail shorter construction periods and lower capital investment, making them attractive for developing regions and off-grid applications [10].

One notable example within this category is the gravitational vortex turbine (GVT), a technology that generates electricity by utilizing the swirling motion of water within a specially designed vortex chamber. In a typical GVT setup, water is directed tangentially into a circular basin, inducing a controlled vortex. The kinetic energy of this vortex is then captured by a centrally located runner, which drives a generator. Due to their compact design, ease of installation, and minimal environmental footprint, GVTs are particularly well suited for decentralized electrification, especially in remote or rural areas with limited access to centralized energy infrastructure [11].

Despite clear advantages in sustainability and accessibility, GVTs face notable technical challenges, especially regarding energy-conversion efficiency. Reported performance levels vary widely, from as low as 13.4% to as high as 82%, depending on site-specific and design-related factors [12,13]. Among the most influential parameters are the geometry of the vortex basin, the shape and slope of the inlet channel, and the design of the turbine runner [14]. Of these, the configuration of the inlet channel plays a particularly critical role, as it directly affects the angular momentum of the incoming flow and, in turn, the strength and stability of the vortex, which are key determinants of the system's overall efficiency and reliability.

Research on GVTs has grown steadily in recent years, driven by the demand for sustainable, low-impact hydropower technologies that are adaptable to decentralized contexts. Studies have shown that these turbines can operate efficiently in sites with very low head, making them a viable option for rural communities or regions with limited infrastructure. Significant progress has been made in understanding flow behavior within the vortex basin, particularly regarding the influence of inlet channel design, basin geometry, and runner characteristics on system efficiency [12–14]. However, important technical challenges remain, such as optimizing angular momentum, stabilizing the vortex under

varying flow conditions, and improving energy performance, which still varies considerably across prototypes. From an environmental perspective, although their ecological footprint is significantly smaller than that of conventional dams, local impacts on aquatic fauna, alteration of microhabitats, and sediment management still require more systematic assessment. Current trends in the literature point toward multidisciplinary approaches that combine computational simulations, laboratory experiments, and field validation. Additionally, there is growing interest in the use of biomimetic principles and designs inspired by nature or ancestral hydraulic systems to enhance the performance and sustainability of these turbines.

This study proposes an inlet channel design for GVTs inspired by the spiral-shaped *ojos* of the ancient Nazca culture of Peru. These structures form part of the aqueduct system known as *puquios*, a remarkably advanced method for managing water in one of the driest regions on Earth [15,16]. The spiral configuration served several functional purposes: allowing maintenance access, enhancing airflow for ventilation, and facilitating continuous, controlled water circulation into underground canals [15]. The behavior observed in these ancient systems, particularly their ability to guide and sustain rotational flow, offers valuable insights for contemporary hydropower design.

By applying the spiral concept to the GVT inlet channel, it is expected that the angular momentum of the incoming water can be increased in a more controlled manner, which could result in a more stable and stronger vortex within the turbine basin and, consequently, improved energy-conversion efficiency of the system. The adaptation of this ancient engineering principle to the modern context of renewable energy exemplifies how traditional knowledge can serve as the basis for innovative solutions for sustainable development.

Accordingly, this research explores the potential of incorporating a Nazca-inspired spiral geometry into the inlet channel of a gravitational vortex turbine to enhance vortex formation and system performance while providing a methodological framework for design exploration. A parametric inlet configuration based on the geometry of the puquios is developed, and its hydraulic behavior is evaluated through computational fluid dynamics (CFD) simulations, with key geometric parameters, namely the number of turns and the inclination angle, optimized using response surface methodology. The optimal inlet is then combined with two runner configurations and assessed numerically, before being fabricated and experimentally tested in a laboratory scale prototype to validate the numerical predictions.

By addressing efficiency and flow structuring challenges through this innovative hydraulic design, the study demonstrates that a Nazca-inspired spiral inlet can generate circulation levels comparable to those of an optimized wrap around channel under similar low-flow conditions, while producing a broader and more symmetric vortex that promotes smoother torque transfer to the runner. Beyond immediate performance metrics, the work highlights the value of integrating ancestral engineering principles with modern computational and experimental tools to advance decentralized and environmentally sustainable hydropower technologies and to inform future methodological and conceptual development in gravitational vortex turbine design.

2. Materials and Methods

2.1. Geometry of the Gravitational Vortex Turbine

From a technical standpoint, GVTs are low-head hydropower systems designed to generate electricity by harnessing the rotational motion of water in a free-surface vortex. These systems are particularly suited for decentralized applications due to their compact design and minimal environmental impact. A typical GVT consists of four main components: (i) the inlet channel, which introduces water into the system in tangential or spiral

manner to generate angular momentum; (ii) the vortex basin or chamber, which may be cylindrical or conical where the vortex develops and stabilizes; (iii) the runner, positioned vertically at the vortex core, which extract mechanical energy from the swirling flow; and (iv) the electric generator, which converts this mechanical energy into electricity. Figure 1 presents a representative configuration of a GVT, highlighting these key structural and functional elements.

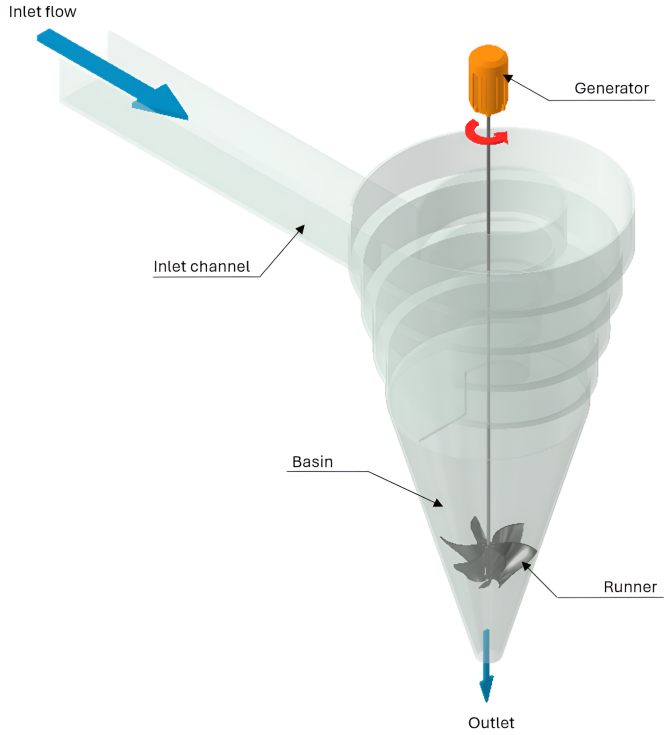


Figure 1. Gravitational vortex turbine (GVT) components.

Several design variations have been proposed in the literature, with particular emphasis on the geometry of the inlet channel and the basin, as these elements critically affect vortex strength and stability. Spiral or enveloping inlet channels are commonly employed to induce rotational flow, while chamber geometry influences the distribution and confinement of the vortex. The interaction between vortex and runner is central to the system's performance; however, many designs still face challenges in achieving high efficiency due to mismatches between flow patterns and runner geometry. As a result, research efforts continue to focus on optimizing both the hydraulic design of channel and chamber, as well as the mechanical design of the runner, to improve overall energy conversion in decentralized, environmentally responsible applications.

The inlet channel plays a crucial role, as it defines the characteristics of the incoming flow before it reaches the basin. Its geometry directly affects angular momentum, flow symmetry, and energy distribution, all of which are essential for achieving a stable and efficient vortex. In this study, the inlet channel design is inspired by the spiral geometry of the *ojos de agua* from the ancient Nazca culture (Peru). These spiral-shaped surface openings are part of the underground aqueduct system known as *puquios*. Typically built with stone or earth, they feature a descending spiral ramp that leads to the subterranean channel. Their distinctive geometry was not only functional but also a remarkable example of pre-Columbian hydraulic engineering.

Functionally, the *ojos de agua* served multiple purposes. First, they allowed direct access to the subterranean channels for maintenance and cleaning, which was essential to ensure the continuous flow of water in a desert environment. Second, their open spiral

shape facilitated natural ventilation, improving airflow through the tunnels and helping to regulate water quality. Third, the spiral design enhanced the movement of air and water, promoting circulation and possibly increasing the efficiency of water capture and distribution through gravitational flow. These combined functions made the *ojos* a key component of the Nazca water-management system, allowing sustainable access to groundwater across dry and rocky terrains. Figure 2 illustrates one of these *ojos*, highlighting the characteristic geometry that informed the parametric design of the inlet channel in this research. By applying these ancestral hydraulic principles, the channel aims to enhance vortex formation and improve overall energy conversion efficiency.



Figure 2. Nazca *ojos de agua*.

This study focused on an experimental prototype, and as such, the design was constrained by several factors. The primary limitation was imposed by laboratory conditions, as the channel had to be dimensioned to fit within the facilities of the Alternative Energy Research Group (GEA), University of Antioquia, where the experimental tests were conducted. Additionally, the available infrastructure played a key role in defining the prototype's scale, ensuring compatibility with the existing hydraulic channel and water pumps. Beyond these physical constraints, hydrodynamic behavior was also considered during the design process. The flow velocity was set to generate a stable vortex while avoiding excessive speeds that could introduce unwanted turbulence, ensuring controlled and predictable motion within the basin.

To adapt the Nazca-inspired geometry to the prototype conditions, certain modifications were necessary. One key adjustment was the reduction of the inclination angle to prevent the spiral from closing too rapidly, which could have compromised the size of the basin. Another important modification involved narrowing the channel width, a strategy that maximized the available space within the experimental setup. This adaptation allowed the flow to complete up to four full turns before reaching the basin, ensuring that essential geometric relationships were preserved while making the experimental results representative of a full-scale turbine.

The inlet channel design was developed using a parametric approach, enabling controlled variations in key geometric parameters such as the number of turns (N) and the inclination angle (θ), with the goal of optimizing vortex formation. Despite these variations, certain baseline dimensions were maintained across all configurations. The channel width was set at 108.5 mm and the depth at 88 mm. For the basin, a conical geometry was selected, following recommendations from previous studies indicating that this configuration maximizes turbine efficiency. The upper basin diameter coincides with the final channel diameter to ensure a smooth transition, while the discharge chamber diameter and the cone height varied with each configuration depending on both geometric parameters. Across all

cases, the discharge diameter ranged from 26.23 mm to 41.02 mm, and the cone height from 439.96 mm to 655.35 mm, ensuring a uniform flow towards the discharge. This configuration facilitated a more efficient distribution of energy within the system. It should be noted that the final dimensions of the channel were determined primarily based on the available space for construction and experimental testing in the laboratory, rather than as a result of hydraulic stability criteria. The physical constraints of the experimental environment limited the channel's length and radius of curvature, necessitating the adaptation of the original design inspired by the Nazca puquios to a manageable scale. Consequently, the selection of the slope and other dimensions became a compromise between maintaining the geometric fidelity of the concept and accommodating the laboratory's spatial conditions. This approach allowed the overall integrity of the spiral geometry and vortex formation to be preserved, but it implies that certain flow characteristics, such as core concentration or the distribution of tangential velocities, might differ from those obtained in a larger-scale prototype or under unconstrained conditions. Therefore, the experimental results qualitatively reflect the behavior of the design, while the exact magnitudes of efficiency or circulation could vary in full-scale implementations.

The turbine model was optimized using design of experiments (DOE) and RSM. This approach enabled a systematic evaluation of the geometric configuration, focusing specifically on two influential factors: number of turns in the inlet channel and inclination angle (Figure 3).

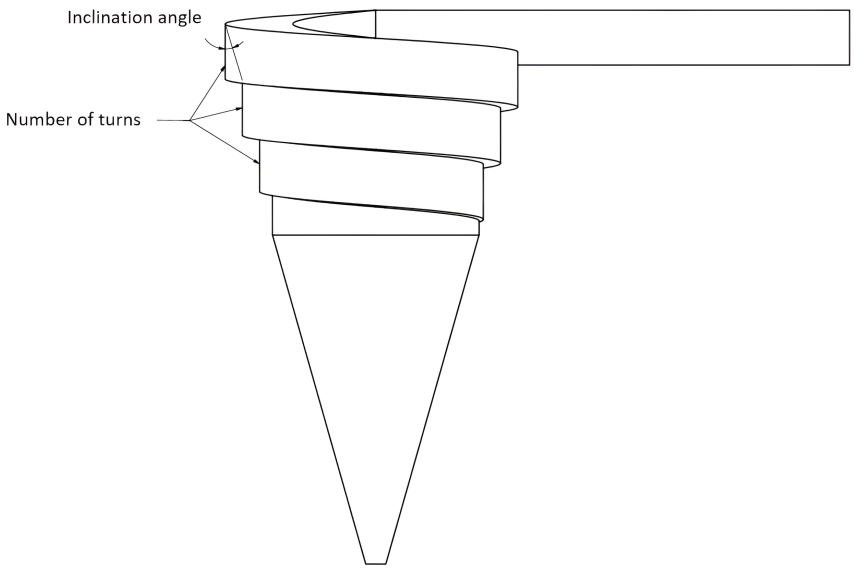


Figure 3. Geometric factors considered in the optimization process: number of channel turns (N) and inclination angle (θ).

2.2. Statistical Analysis and Optimization

The optimization process aimed to identify the inlet channel geometry that would maximize vortex circulation within the system, since this parameter is directly associated with the stability and efficiency of the rotational flow in the chamber. To achieve this objective, a structured experimental design was applied in conjunction with RSM, which is a set of statistical techniques used to model and optimize a response variable that is influenced by multiple independent parameters [17].

This methodology was used to systematically analyze the relationship between the geometric configuration of the channel, particularly N and θ, and the resulting circulation (Γ) values within the vortex. RSM allows for the evaluation of both individual effects and interactions between factors, typically requiring the development of a second-order

regression model. Its primary advantage lies in its ability to predict system behavior beyond the experimental domain while identifying optimal conditions using a limited number of simulations. This results in a significant reduction in computational cost. Due to these capabilities, this methodology has been widely adopted in hydrodynamic analysis and energy system optimization studies [18,19].

A full factorial experimental design with 3^2 treatments was employed to evaluate the influence of two geometric parameters on vortex development: N and θ of the inlet channel. These parameters were selected for their critical role in shaping the flow path and inducing angular momentum, which are essential for generating a stable and coherent vortex. Each factor was assessed at three levels: $N \in 2, 3, 4$ and $\theta \in 13°, 15°, 17°$. This approach resulted in nine unique combinations, allowing for the systematic evaluation of both main effects and interactions. The different channel geometries corresponding to each treatment are illustrated in Figure 4.

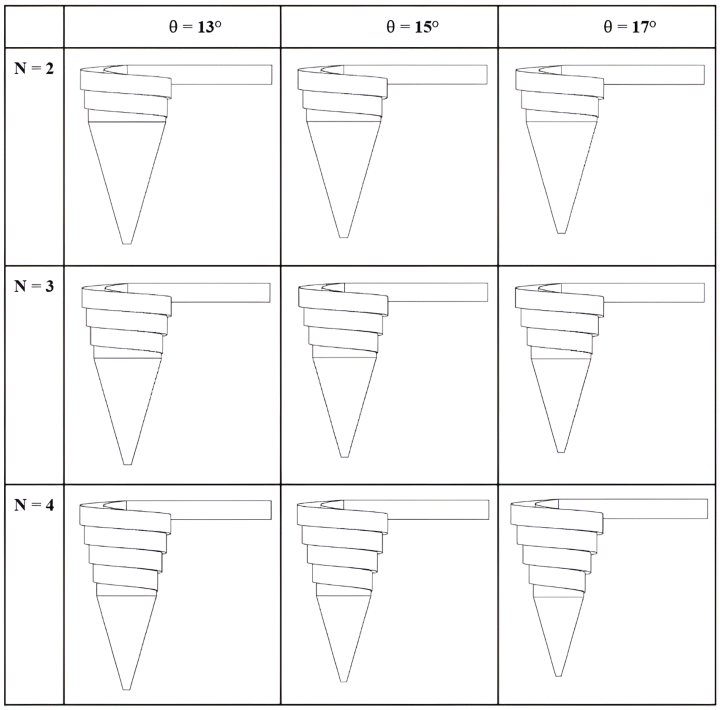


Figure 4. Studied geometries.

The response variable used in this analysis was vortex circulation (Γ), which serves as a direct indicator of vortex strength and coherence. Circulation was calculated on a horizontal plane within the basin by integrating the vorticity field over the defined area. This metric captures the rotational intensity of the flow and is widely applied in hydrodynamic performance assessments of vortex-based energy systems.

To describe the relationship between N, θ, and Γ, a quadratic regression model was fitted. The general form of the response surface model used in this study is represented in Equation (1). This second-order polynomial equation captures the relationships between the response variable and the experimental factors by including linear, quadratic, and interaction terms.

$$\Gamma(N, \theta) = \beta_0 + \beta_1 N + \beta_2 \theta + \beta_{11} N^2 + \beta_{22} \theta^2 + \beta_{12}(N \cdot \theta) \quad (1)$$

where β_0 represents the intercept, β_1 and β_2 correspond to the linear effects, β_{11} and β_{22} capture the quadratic effects, and β_{12} accounts for the interaction between the two factors. The coefficients of the model were estimated using least-squares regression, and their

statistical significance was evaluated to identify which factors had the most significant impact on Γ.

Therefore, to analyze the results of the 3^2 factorial experimental design, an analysis of variance (ANOVA) was performed to evaluate the statistically significant influence of the geometric factors and their interactions on the response variable, which in this case was the vortex circulation. A significance level of $\alpha = 0.05$ was used, meaning that effects with a p-value lower than 0.05 were considered statistically significant. Additionally, the coefficients of determination R^2 and adjusted R^2_{adj} were calculated to quantify the degree of fit of the model to the experimental data. A high adjusted R^2_{adj} value indicates that the model adequately explains the observed variability, taking into account the number of terms included.

For the ANOVA results to be valid, certain statistical assumptions must be verified: normality of residuals, homogeneity of variances (homoscedasticity), and independence of errors. These assumptions were assessed through normal probability plots, residuals versus fitted values analysis, and complementary statistical tests. Only when these criteria are met can the significant effects be reliably interpreted and the model used to make valid predictions and optimizations of the system's hydraulic performance.

All treatment combinations resulting from the full factorial experimental design were evaluated using CFD simulations to predict the system's performance under various factor settings. This simulation-based approach allowed for a detailed analysis of flow behavior and performance metrics without the need for immediate physical prototyping. Based on the analysis of the response surface model and optimization criteria, the configuration identified as optimal was subsequently fabricated and subjected to experimental testing to validate the simulation results and confirm its practical effectiveness.

2.3. CFD Simulation Setup

CFD simulations were performed using ANSYS Fluent 2024 R1, which was selected for its capability to handle complex geometries and accurately solve transient multiphase flow problems, and were carried out in two distinct phases: (i) optimizing the inlet channel and basin geometry without the runner, and (ii) evaluating the runner performance using the previously optimized configuration. The three-dimensional models of the inlet channel, conical basin, and runner were created in Autodesk Inventor 2025 and imported into ANSYS SpaceClaim 2024 R1 for cleaning and simplification, ensuring watertight surfaces and eliminating unnecessary details that could affect the meshing process.

The initial CFD phase focused on optimizing the geometry of the inlet channel and the conical basin, aiming to maximize vortex stability and strength before incorporating the runner. The computational domain for this phase included the inlet channel and the conical basin. A poly-hexcore mesh was generated using ANSYS Meshing 2024 R1 which balances computational efficiency with high resolution in critical areas. Mesh refinements were applied near the inlet, basin walls, and outlet to improve flow capture and boundary layer resolution. The final mesh, shown in Figure 5, exhibited an orthogonal quality with a minimum value of 0.30, a maximum skewness of 0.699, and an aspect ratio that remained below 29.34, ensuring numerical stability and accurate solution convergence.

To ensure that the CFD simulation results were independent of the mesh resolution, a mesh independence study was conducted using three mesh densities: coarse, medium, and fine. Γ was selected as the representative metric to evaluate convergence behavior, as shown in Table 1. Richardson extrapolation was applied to estimate the discretization error, and the mesh convergence index was calculated to quantify numerical uncertainty. The variation in Γ between the medium and fine meshes was found to be less than 2%, while the Grid Convergence Index (GCI) was calculated as 4.341% for the fine-to-medium

comparison and 2.979% for the medium-to-coarse comparison. Moreover, the convergence index, defined as the ratio of successive error reductions, was determined to be 0.989, confirming that the solution resides in the asymptotic range of convergence. Based on these results, the medium mesh, containing 2,094,036 elements, was selected as it offered an optimal trade-off between numerical accuracy and computational cost.

Table 1. Mesh independence study results for circulation (Γ).

Mesh	Elements	Circulation (m^2/s)	Error (%)
Coarse	1,632,798	0.865	–
Medium	2,094,036	0.851	1.645
Fine	2,403,455	0.8415	1.129

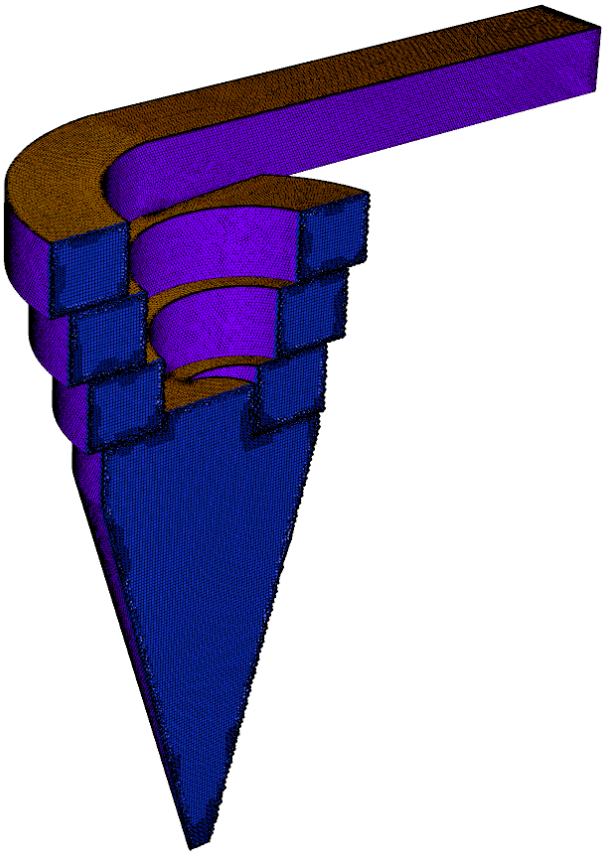


Figure 5. Mesh used for inlet channel and basin optimization.

The boundary conditions were defined to replicate realistic operational conditions. The inlet velocity was imposed at the entrance of the channel, while the bottom outlet was assigned a relative pressure of 0 Pa. The upper surfaces of the channel and basin were designated as open boundaries, also at a relative static pressure of 0 Pa, to allow for unrestricted air movement in and out of the system. The inlet velocity was determined using the methodology proposed by Velásquez [20], which employs the discharge coefficient approach, shown in Equation (2).

$$C_d = \frac{4Q}{\pi d^2 \sqrt{2gH^*}} \tag{2}$$

where C_d represents the discharge coefficient, Q is the volumetric flow rate, d is the outlet diameter, g is the gravitational acceleration (9.81 m/s^2), and H^* is the water height in the

basin. Velasquez proposed an empirical relationship between C_d and the geometric ratio d/D as expressed in Equation (3).

$$C_d = 0.7721 \exp\left(-6.4409 \frac{d}{D}\right) - 0.0464 \quad (3)$$

which was used to compute an inlet velocity of 0.28 m/s for the present simulations.

The fluid in all simulations was modeled as incompressible water, with constant properties defined as density $\rho = 998.2$ kg/m^3 and dynamic viscosity $\mu = 1.003 \times 10^{-3}$ Pa/s. To effectively track the air-water interface, the Volume of Fluid (VOF) model was used, ensuring accurate simulation of the free-surface behavior within the system. The turbulence was modeled using the k–ε RNG approach, which has been extensively validated for swirling and recirculating flows.

The solver was set to a pressure-based, transient formulation with implicit time integration. The Pressure-Velocity Coupling was managed using the PISO (Pressure-Implicit with Splitting of Operators) scheme, which provides stability for transient flows with high swirling intensity. For spatial discretization, second-order upwind schemes were applied to the momentum and turbulence equations to reduce numerical diffusion and improve solution accuracy. The transient simulations were performed using various time steps to ensure numerical stability and accuracy. Table 2 presents the time-step independence study, showing that a time step of $\Delta t = 0.005$ s was optimal, as it resulted in minimal variation in Γ while also maintaining computational efficiency.

Table 2. Time-step independence study results.

Time Step (s)	Circulation (m^2/s)	Error (%)
0.01	0.851	–
0.005	0.8492	0.212
0.0025	0.8467	0.295

A time-step independence analysis was also performed to ensure the accuracy of the transient simulations. Temporal GCI was calculated using results from simulations with time steps of $\Delta t = 0.01$ s; 0.005 s; 0.0025 s. Γ was again used as the reference parameter for comparison. The GCI values obtained were 1.318% for the 0.01 s–0.005 s comparison and 0.946% for the 0.005 s–0.0025 s comparison, indicating minor changes in the solution with decreasing time-step size. Additionally, the time-step convergence index, defined as the ratio of successive relative errors, was found to be 0.997, confirming that the solution is within the asymptotic range of temporal convergence. Based on these results, a time step of 0.005 s was selected as it provides a suitable compromise between accuracy in capturing transient flow behavior and overall computational efficiency.

The convergence of the simulations was evaluated using several criteria. Residuals for continuity and momentum equations were monitored, ensuring they remained below 10^{-3}. Additionally, the evolution of Γ over time was tracked to confirm that the system reached a steady state before data extraction. The circulation was calculated using Equation (4).

$$\Gamma = \int_A \omega \, dA \quad (4)$$

where ω_z represents the local vorticity (rad/s) and A is the horizontal plane over which the integration was performed, located 700 mm below the upper edge of the inlet channel. This metric provided a reliable indicator of vortex strength, ensuring that the optimal geometry selection was based on well-converged results.

All numerical simulations corresponding to the treatment combinations defined by the full factorial experimental design were carried out using the validated CFD setup. Each

simulation represented a unique configuration of the independent variables, enabling the systematic evaluation of their individual and combined effects on the response variable. This comprehensive approach ensured full coverage of the design space and provided the necessary data to construct the response surface model. The use of CFD allowed for a detailed analysis of the transient flow behavior and performance indicators under each experimental condition, without the need for immediate physical testing. The resulting dataset formed the basis for subsequent regression analysis and optimization.

The runner is a critical component of the GVT plays a key role in converting the vortex energy, generated by the water flow, into usable mechanical power. The runner's geometry directly influences the system's ability to capture the vortex energy, affecting both the torque and the stability of the flow inside the basin. An efficient runner design is essential to maximize energy conversion efficiency.

For this study, two runner configurations were selected to evaluate their performance in the system with the optimized inlet channel and vortex chamber geometry. Both configurations were adapted to fit the optimized basin dimensions, with the number of blades standardized to four, and global dimensions (upper diameter 165 mm, height 70 mm) kept consistent. This allowed a direct comparison of the effect of blade shape and configuration. Figure 6 shows the two runner geometries evaluated in this study.

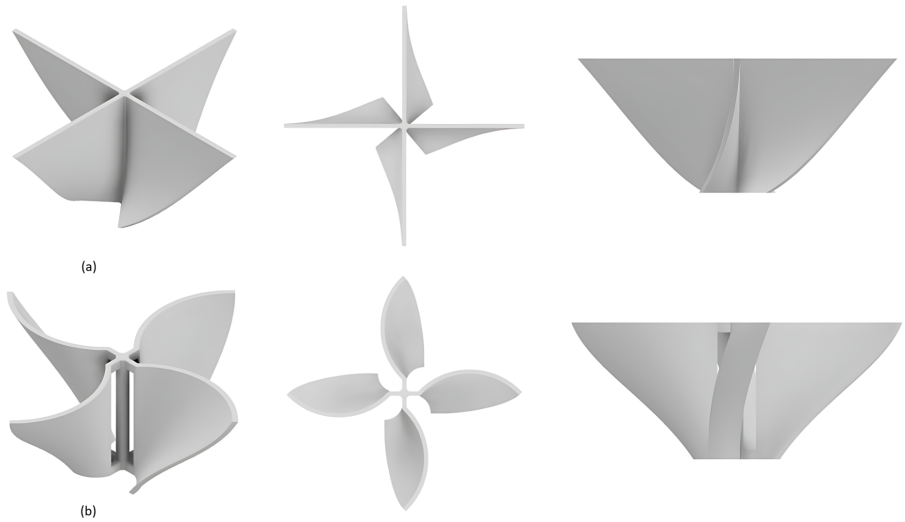


Figure 6. Runner geometries evaluated in this study. (**a**) Runner 1: twisted blades; (**b**) Runner 2: curved cross-flow blades.

The first runner, referred to as Runner 1, was designed with twisted blades, based on research by Edirisinghe et al. [21], who demonstrated that progressively twisted blades enhance energy extraction in vortex turbines. This design included a 50° twist at the base of the blades, and for this study, the design was modified to fit the optimized system by reducing the number of blades from eight to four, while maintaining the key aerodynamic features.

The second runner, referred to as Runner 2, was inspired by the work of Betancour et al. [22], who investigated curved blade geometries with a torsion angle of 55° to improve vortex stability and reduce energy dissipation. This configuration also incorporated cross-flow blades, following the study by Khan [23], which suggested that cross-flow blades facilitate more efficient water movement along the vortex, reducing energy losses. As with Runner 1, the general dimensions were standardized, but modifications were made to the curvature of the blades to assess its impact on performance.

The selection of these two configurations was based on their respective advantages in converting kinetic energy and stabilizing the vortex flow, aiming to evaluate which design

would yield the highest efficiency under similar hydraulic conditions. The analysis focused on the blade shape, ensuring that modifications did not introduce variables beyond the runner geometry.

After optimizing the inlet channel and basin, numerical simulations were performed to evaluate the hydrodynamic performance of the two different runner configurations. The objective was to determine how each design interacted with the vortex flow and to assess its efficiency in converting hydraulic energy into mechanical power. The computational domain used in this phase incorporated the optimized channel and basin geometry and was split into two regions: a stationary section that included the inlet channel and upper part of the basin, and a rotating region containing the runner and lower basin area. This division enabled the simulation of rotational effects using a moving reference frame (MRF) approach. Figure 7 shows the computational domain used for these simulations. The runners were positioned at 60% of the cone height, measured from the upper edge of the cone to the center of the runner height, ensuring geometric consistency across all simulations.

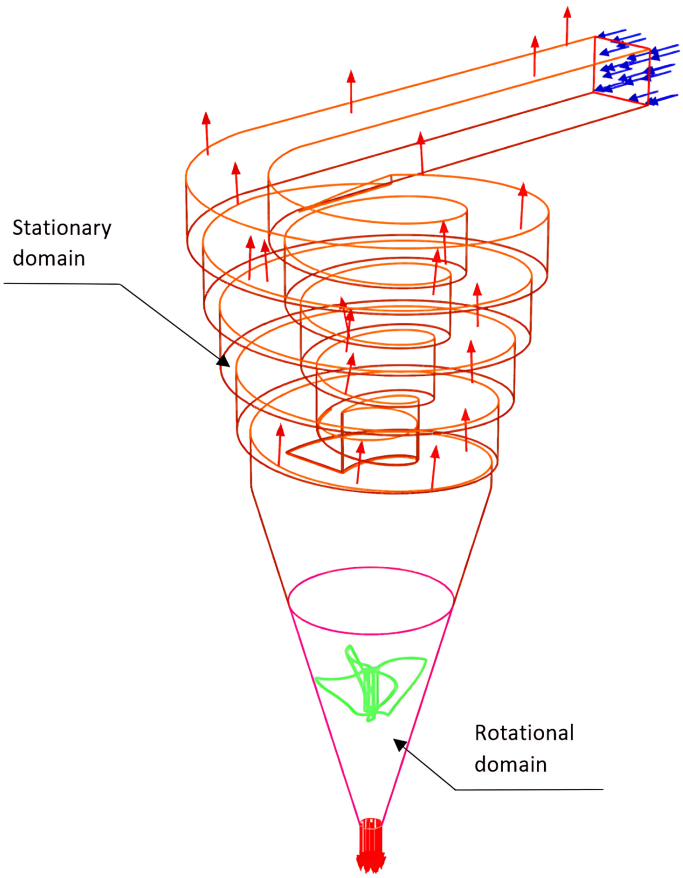


Figure 7. Computational domain for runner evaluation, showing the stationary and rotating regions.

The mesh applied to the computational domain followed the same poly-hexcore approach used in the previous simulations. Refinements were made in the area around the runner to accurately capture the detailed interactions between the vortex and the blades, ensuring a precise representation of flow characteristics. The mesh quality was validated through standard metrics, maintaining numerical stability and reliable solution accuracy.

The velocity at the inlet was determined using the same discharge coefficient methodology that was applied in the inlet channel and basin simulations. A uniform velocity profile of 0.15 m/s was established. At the outlet, a zero-pressure condition was applied to allow unrestricted flow discharge. To analyze the performance of the runners under

different operational conditions, simulations were conducted at rotational speeds (ω) of 0 rpm; 50 rpm; 75 rpm; 100 rpm; 125 rpm; 150 rpm.

The turbulence model selected for this analysis was the realizable k–ε model, selected for its effectiveness in managing swirling and recirculating flows. To accurately model the air-water interface, VOF method was employed to capture the dynamics of the free surface. The solver was set to a pressure-based, transient formulation, with the PISO scheme applied for pressure-velocity coupling. Second-order upwind discretization was used for the momentum and turbulence equations to improve numerical accuracy.

To evaluate the performance of each runner configuration, torque values were recorded for each rotational speed. The mechanical power output (P) was calculated using Equation (5).

$$P = T\,\omega, \tag{5}$$

where T is the torque (Nm) and ω is the angular velocity (rad/s). The efficiency (η) of the system was then calculated using Equation (6).

$$\eta = \frac{P}{\rho\, g\, Q\, H}, \tag{6}$$

where ρ represents the water density, g is gravitational acceleration, Q is the volumetric flow rate, and H is the available head. In this study, H is defined as the vertical distance between the end of the inlet channel (i.e., the outlet of the spiral) and the runner center, which represents the effective hydraulic drop used to calculate the available power.

It is important to highlight that this study using CFD was conducted with certain simplifications that, while limiting the absolute accuracy of the results, provide valuable insights into the general flow behavior and relative efficiency of different configurations. These simplifications include the idealization of boundary conditions, the assumption of hydraulically smooth walls, the omission of mechanical components such as the runner shaft, and limited mesh resolution. Such choices significantly reduce computational cost and simulation time, enabling a systematic exploration of multiple geometric parameters and operating scenarios through design of experiments. However, these same simplifications may lead to overestimation of efficiency and do not fully capture small-scale complex phenomena, such as local turbulence, flow separation, or wall–flow interactions, which directly affect angular momentum transfer and the effective torque on the runner. Therefore, while CFD simulations provide a solid framework for trend analysis and parameter optimization, the results should be interpreted as indicative and validated through physical experiments to ensure applicability under real operating conditions.

2.4. Experimental Setup

To validate the numerical predictions, an experimental test bench incorporating a GVT was built at laboratory scale. The prototype reproduced, as closely as practical, the optimized inlet channel and basin geometry used in the CFD simulations. The setup ran as a closed, recirculating water loop comprising an upper supply tank, a lower reservoir tank, a centrifugal pump (30A-15W, IE2 (Ignacio Gómez IHM, Medellín, Colombia)), the Nazca-inspired inlet channel, the conical basin, and the runner. The lower tank collected the discharged water, which was then pumped back to the upper tank. All tests were conducted at a constant flow rate of 1.4 L/s, matching the operating conditions used in the CFD simulations.

The inlet channel and basin were constructed from 5.5 mm thick transparent acrylic sheets, laser-cut and bonded with adhesive. This material was selected for its optical transparency, which enables direct visualization of vortex formation, its mechanical stiffness and chemical resistance under repeated wet operation, and its favorable cost–manufacturability balance. The runners were manufactured using fused deposition modelling (FDM) 3D printing with 1.75 mm PLA filament, a layer height of 0.2 mm, 20% infill in a grid pattern and an extrusion temperature of 210 °C. This approach ensured adequate geometric accuracy, low production cost, reduced rotational inertia, and sufficient stiffness for laboratory-scale hydrodynamic testing. However, no post-processing or surface smoothing was applied, and the inherent surface roughness of the FDM-printed PLA was not quantified. From a physical standpoint, this roughness increases skin-friction drag and promotes early transition of the boundary layer, generating higher viscous losses along the blade surfaces. The resulting reduction in the tangential component of the flow velocity decreases the effective transfer of angular momentum to the runner and, consequently, the torque-transfer efficiency. Additionally, micro-roughness can induce local flow separation and small-scale turbulence, dissipating kinetic energy before it is converted into useful mechanical power. These effects were not considered in the current CFD simulations, which assumed hydraulically smooth walls and idealized conditions, likely contributing to the overestimation of efficiency in the numerical results.

Instrumentation was implemented to monitor the system's hydraulic and mechanical performance. To measure the volumetric flow rate Q, an electromagnetic flow-meter (Siemens SITRANS FM MAG 5100 W (Siemens, Munich, Germany)) was used, ensuring that the inlet conditions stayed within pre-defined tolerances during each test. T and ω were recorded with a rotary torque sensor with an integrated encoder (FUTEK TRS 605-FSH02057, Irvine, CA, USA) mounted coaxially on the shaft. Data acquisition was performed using dedicated software at a sampling frequency of 0.1 Hz, providing time series of Q, T, and ω for each operating point to calculate the mechanical power output (see Equation (5)). The hydraulic efficiency (η) was then computed according to Equation (6), using the measured flow rate and the net head H.

To evaluate the performance of the runners under different operating conditions, the experiment was conducted at constant flow rate while a variable load was applied to the runner. Load control was achieved through an active electrical brake based on a Pololu 4741 micromotor (Pololu Robotics and Electronics, Las Vegas, NV, USA), mounted coaxially with the shaft and driven in opposition to the direction of rotation, effectively acting as a controllable energy absorber. The brake current was adjusted in discrete steps using a variable frequency drive (VFD) and power supply, allowing precise control of torque resistance and rotational speed. At each load step, the system was allowed to reach steady conditions before recording data for 5, and the procedure was repeated until the runner stopped, generating the $\eta(\omega)$ curves used for comparison with CFD predictions. Figure 8 illustrates the full experimental setup used in this study.

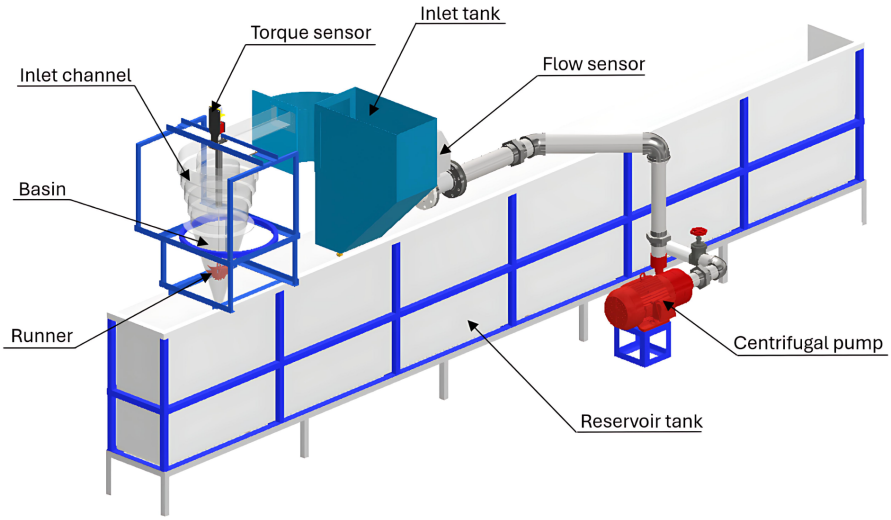


Figure 8. Experimental setup for GVT validation tests.

3. Results and Discussion

3.1. CFD Results

The CFD simulation reveals the fluid dynamic behavior inside the turbine. It is evident that the spiral inlet channel plays a fundamental role by imposing a velocity field with controlled vorticity from the inlet, transforming a predominantly axial flow into a well–organized rotational flow and minimizing the generation of turbulence. As shown by the streamlines in Figure 9a, this geometry induces a quasi-laminar helical trajectory which, as it descends along the conical section, is strictly governed by the principle of conservation of angular momentum. The progressive reduction of the local radius of rotation r forces an acceleration of the fluid from mean inlet velocities on the order of 1.14 m/s up to maximum values of 2.28 m/s at the lower outlet, satisfying the relationship shown in Equation (7).

$$L = mv_\theta r = \text{constant} \tag{7}$$

where L is the angular momentum, m is the mass of the fluid element, v_θ is the tangential component of the velocity, and r is the local radius of rotation.

This behavior defines the velocity profile shown in Figure 9b, in which the kinetic energy is concentrated near the periphery of the conduit, while the central region exhibits null tangential velocities ($v_\theta = 0$ m/s), evidencing the formation of a stable air core. The coexistence of a high-velocity peripheral zone and a nearly stagnant axis confirms the transition toward a free-vortex regime, characterized by the dependence $v_\theta \propto 1/r$, which constitutes an optimal condition for energy extraction by the turbine without penalties due to excessive viscous dissipation.

Dynamically, the intense peripheral rotation satisfies the Euler equation for radial equilibrium in cylindrical coordinates, as shown in Equation (8).

$$\frac{1}{\rho}\frac{\partial p}{\partial r} = \frac{v_\theta^2}{r} \tag{8}$$

where ρ is the fluid density, p is the static pressure, r is the radial coordinate, and $v\theta$ is the tangential velocity component.

Whose physical consequence is directly reflected in the pressure distribution shown in Figure 9c. The centrifugal acceleration associated with the high tangential velocities induces a combined hydrostatic and dynamic pressure load of up to 1.91×10^3 Pa on the

outer wall, which constitutes a critical design parameter for the structural sizing of the turbine casing.

Conversely, the vortex core develops a pronounced pressure depression, reaching a suction level of -9.12×10^2 Pa along the central axis. This radial pressure gradient is not a numerical artifact but a direct manifestation of the balance between centrifugal forces and the pressure field. It physically validates the system's ability to sustain a stable air–water interface, a necessary condition for efficient discharge and for preventing backpressure-induced flow separation or intermittent vortex collapse that would otherwise degrade turbine performance.

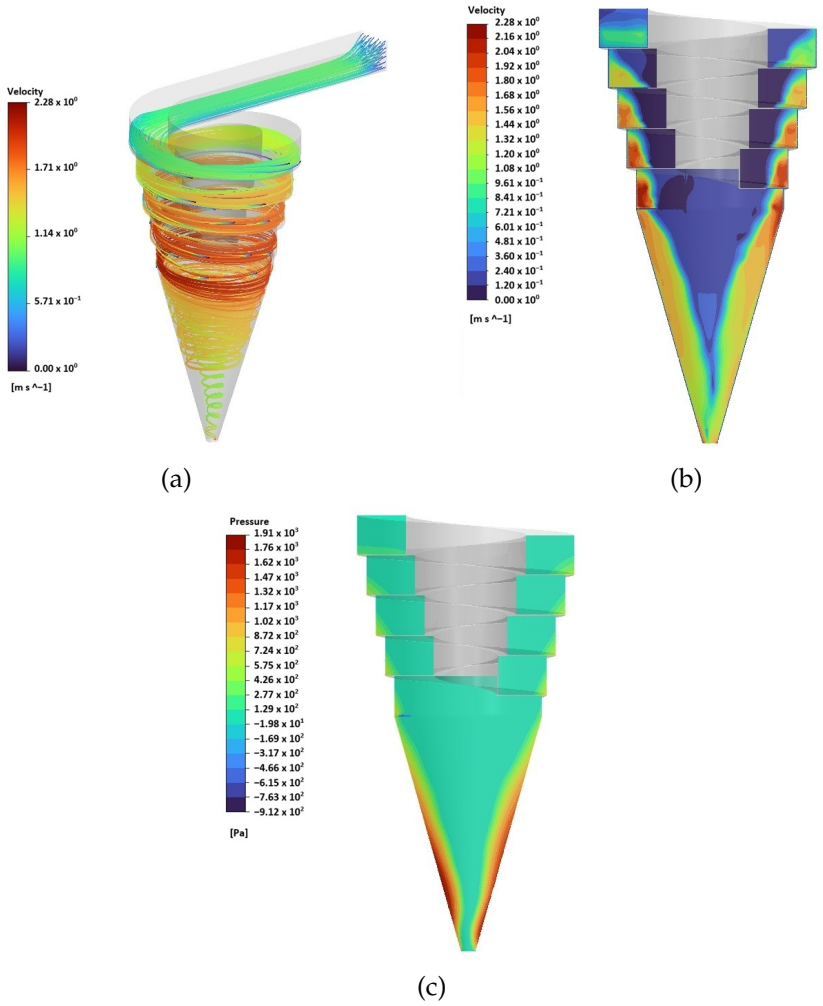


Figure 9. Results of the CFD analysis of a gravitational vortex turbine without runner. (**a**) Streamline distribution inside the turbine, (**b**) Velocity profile across the turbine cross section (**c**) Pressure profile across the turbine cross section.

The incorporation of runner 1 into the simulation transforms the system behavior from a purely gravitational flow regime into one governed by dynamic interaction for power transfer. An analysis of Figure 10a reveals a substantial increase in the maximum velocity magnitude, reaching 5.07 m/s. This value does not represent a global mean velocity but rather a localized and physically critical acceleration in the blade region, where the reduction of the effective flow passage area forces the fluid to accelerate due to a Venturi-like effect, thereby maximizing momentum exchange with the turbine.

This phenomenon is further corroborated in Figure 10b, where the velocity profile exhibits pronounced stratification: a slower flow in the upper region caused by the hydraulic resistance imposed by the runner, and peak velocities concentrated exclusively in

the energy extraction zone. This spatial redistribution of kinetic energy indicates that the runner actively reshapes the internal flow field, promoting controlled acceleration where torque generation is most efficient.

Finally, the energetic validation is observed in the pressure distribution shown in Figure 10c. The reduction of the maximum wall pressure to 1.45×10^3 Pa, compared to 1.91×10^3 Pa for the runnerless configuration, quantitatively demonstrates that a significant fraction of the fluid's pressure and potential energy is being effectively converted into mechanical work on the shaft. This behavior is fully consistent with the principle of energy conservation as formalized by Bernoulli's equation extended to turbomachinery, where the pressure drop across the runner represents useful work extraction rather than dissipative loss.

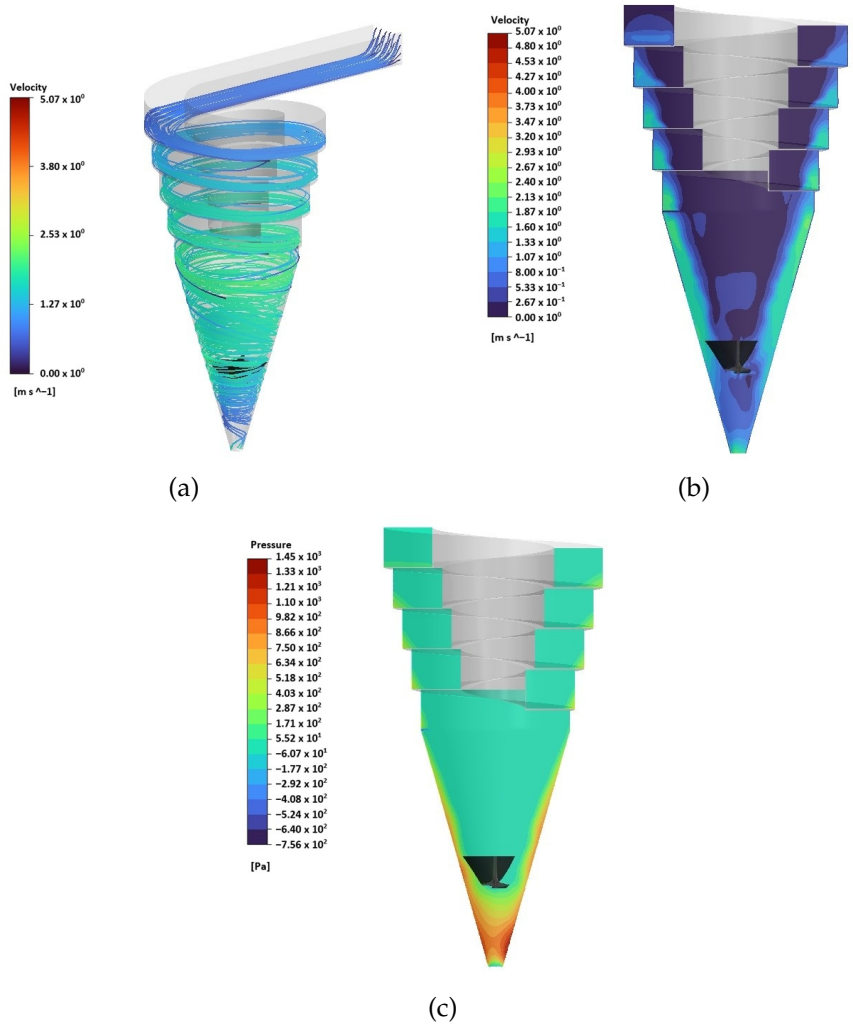


Figure 10. Results of the CFD analysis of a gravitational vortex turbine with runner 1. (**a**) Streamline distribution inside the turbine, (**b**) Velocity profile across the turbine cross section (**c**) Pressure profile across the turbine cross section.

The CFD analysis of runner 2 reveals a distinctive hydrodynamic behavior characterized by a higher capacity for kinetic energy conversion compared to the previous models. As observed in Figure 11a,b, the maximum fluid velocity is limited to 3.85 m/s, a value significantly lower than the 5.07 m/s recorded with runner 1. This reduction does not imply a loss of performance; rather, it technically indicates that runner 2 imposes a stronger hydrodynamic reaction or resistance, extracting momentum from the flow more aggressively and preventing its free acceleration through the blade passages.

This efficient hydraulic braking effect is corroborated in Figure 11c, where the maximum wall pressure remains at 1.44×10^3 Pa, confirming continued extraction of pressure and potential energy, while the minimum pressure drops sharply to -9.93×10^2 Pa. This latter value, being the most intense suction observed across all simulations, indicates that the runner 2 geometry strengthens the vorticity of the central core, thereby maximizing the available pressure differential for torque generation.

From a turbomachinery standpoint, this behavior is consistent with a higher flow deflection and a larger change in angular momentum across the runner, as formalized by the Euler turbine equation. While this enhances energy extraction efficiency, it also drives the operating point closer to cavitation inception or air-core instability limits, highlighting a critical design trade-off between torque maximization and hydraulic stability.

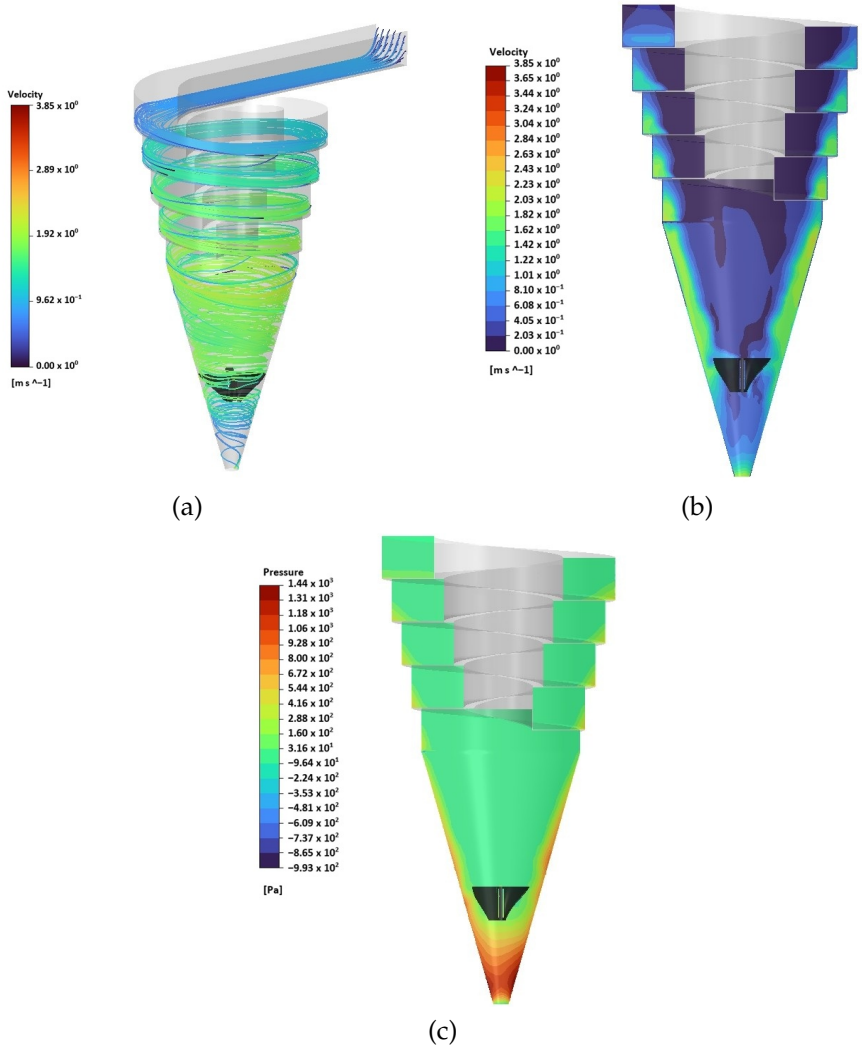


Figure 11. Results of the CFD analysis of a gravitational vortex turbine with runner 2. (**a**) Streamline distribution inside the turbine, (**b**) Velocity profile across the turbine cross section (**c**) Pressure profile across the turbine cross section.

The computational study validates the hydrodynamic suitability of the spiral inlet channel and the conical outlet for the generation of a stable gravitational vortex, demonstrating that the efficiency of energy conversion depends critically on the runner geometry. The comparative analysis reveals that, while runner 1 promotes flow acceleration, reaching peak velocities of 5.07 m/s and effectively behaving as a low-resistance nozzle, runner 2 exhibits superior performance in terms of power transfer.

The ability of runner 2 to limit the maximum velocity to 3.85 m/s while simultaneously generating the strongest suction in the vortex core (-9.93×10^2 Pa) provides clear physical evidence of enhanced momentum extraction through effective hydraulic braking and a more robust coupling with the vortex structure. This dual effect indicates a larger pressure drop across the runner and a greater change in angular momentum imparted to the shaft.

Consequently, it is concluded that the runner 2 configuration optimizes the balance between the available pressure drop and torque generation, while minimizing the residual kinetic energy at the outlet compared to runner 1. From a turbomachinery perspective, this behavior reflects a more favorable matching between the vortex flow field and the runner blade geometry, thereby maximizing useful work extraction and overall hydraulic efficiency.

The analysis of the fluid–structure interaction in runner 1 (Figure 12a,b) reveals a power generation mechanism dominated by a strong pressure gradient, but constrained by internal flow instabilities. The pressure distribution over the blades shows an effective loading, with maxima of 1.45 kPa on the pressure (leading) side and suction levels of −756 Pa on the trailing side, thereby generating the driving torque required for shaft rotation.

However, the velocity vector field analysis (Figure 12b) exposes significant aerodynamic inefficiencies. The presence of closed recirculation zones within the inter-blade passages indicates flow separation, implying that the current blade curvature fails to guide the fluid smoothly along the blade surfaces. This separation induces internal turbulence and secondary flows that dissipate a non-negligible fraction of the incoming kinetic energy, whose peak magnitude reaches 5.07 m/s, before it can be effectively converted into useful mechanical work.

From a turbomachinery perspective, these flow detachment phenomena reduce the effective change in angular momentum imparted to the runner, thereby degrading hydraulic efficiency and increasing entropy production within the runner. Consequently, although runner 1 is capable of generating torque through a favorable pressure differential, its overall performance is penalized by suboptimal blade geometry that promotes flow instability and energy dissipation rather than coherent momentum transfer.

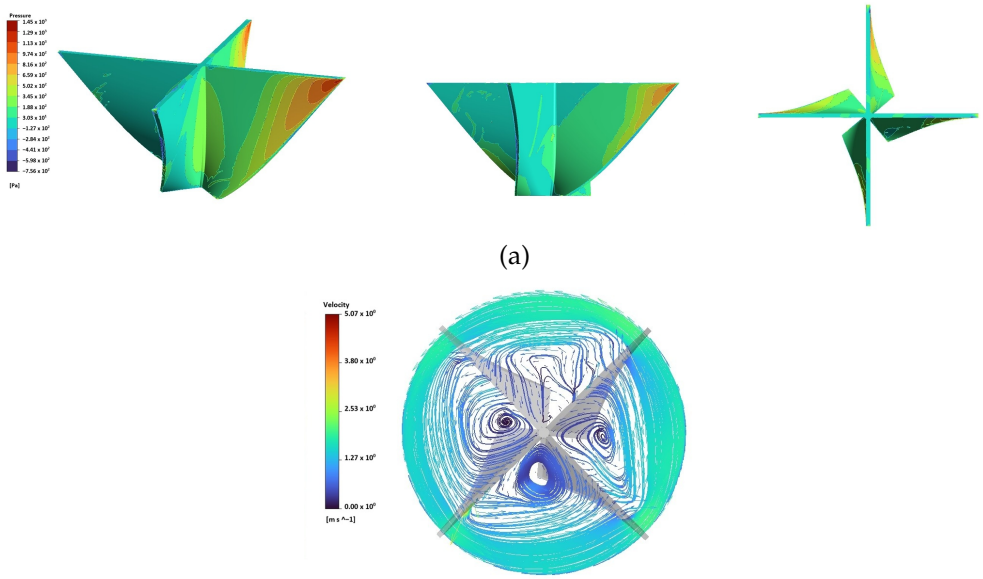


Figure 12. Results of the CFD analysis of a gravitational vortex turbine with runner 1. (**a**) Pressure distribution on runner 1, (**b**) Velocity profile across the runner cross section.

The detailed analysis of runner 2 (Figure 13a,b) demonstrates clear hydrodynamic superiority attributable to the curvature of its blades, which optimizes the energy conversion mechanism through lift-based forces. The pressure distribution (Figure 13a) exhibits an amplified differential: while the pressure side sustains an effective load of 1.44 kPa, the suction side develops a critical depression of −993 Pa, the most intense observed in the entire study, thereby maximizing the resulting torque through a Bernoulli-driven mechanism.

Complementarily, the internal hydrodynamics (Figure 13b) reveal a flow field that remains more closely attached to the blade surfaces, with significantly reduced boundary-layer separation compared to runneer 1. This indicates that the blade curvature provides a smoother pressure gradient and a more favorable incidence angle for the incoming vortex flow, mitigating adverse pressure gradients that typically trigger flow detachment.

The predominance of reduced velocities along the streamlines, with peak values limited to 3.85 m/s, further confirms that the curved geometry effectively "captures" the kinetic energy of the vortex and converts it into useful mechanical work. By suppressing excessive flow acceleration, the design minimizes losses associated with turbulence, secondary flows, and slip effects that characterized the previous configuration. From a turbomachinery perspective, this behavior reflects a more efficient lift-to-drag ratio and a larger effective change in angular momentum across the runner, thereby enhancing overall hydraulic efficiency and torque production.

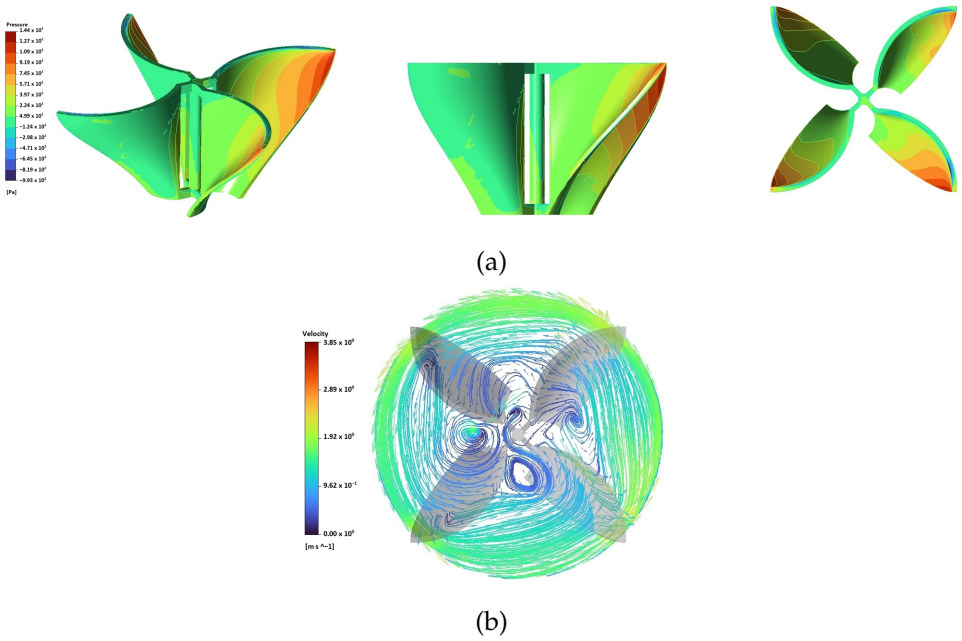


Figure 13. Results of the CFD analysis of a gravitational vortex turbine with runner 2. (**a**) Pressure distribution on runner 1, (**b**) Velocity profile across the runner cross section.

The direct correlation between vortex symmetry and the increase in torque transfer is quantitatively supported by the optimization of the pressure differential and the efficiency of kinetic energy conversion. Unlike the unstable behavior observed in runner 1, the hydrodynamic symmetry achieved by the geometry of runner 2 promotes superior flow attachment, which enables the development of a critical suction pressure of −993 Pa on the blade suction side, exceeding by approximately 31% the suction capacity of the previous design (−756 Pa).

This strengthening of the pressure differential (ΔP) constitutes numerical evidence of an increase in lift force and, consequently, in driving torque. Furthermore, the stability of the vortex minimizes losses due to turbulent dissipation, a fact that is validated by the reduction in the maximum discharge velocity from 5.07 m/s (runner 1) to 3.85 m/s

(runner 2). This velocity decrement of 1.22 m/s confirms that, owing to the improved flow symmetry, a larger fraction of the available kinetic energy has been effectively transformed into mechanical work on the shaft. From a physical standpoint, a more symmetric vortex leads to a more uniform circumferential distribution of tangential velocity and pressure, which results in more even blade loading and reduced periodic force imbalances. This uniformity mitigates torque oscillations and enhances the effective angular momentum transfer to the runner.

An important limitation of the present study is the largely sequential design approach adopted for the inlet and the runner, despite the strong physical coupling between the vortex structure generated by the inlet geometry and the aerodynamic loading developed on the runner blades. From a physical standpoint, the inlet not only determines the magnitude of circulation, but also the radial and tangential velocity distributions, turbulence levels, and the incidence angles delivered to the runner, which directly control torque generation and local losses. In this context, designing or evaluating the runner on the basis of a flow field induced by a fixed inlet can lead to mismatches between the actual inflow angles and the blade geometry, resulting in incidence losses, flow separation, and reduced angular momentum transfer, even when the inlet itself produces a strong vortex. For these reasons, although the present work adopts this sequential framework primarily for methodological clarity and experimental feasibility, it is explicitly recognized that a fully coupled optimization, in which the inlet geometry and runner parameters are varied simultaneously, would constitute a more physically consistent approach and is likely to yield higher overall efficiency.

3.2. Optimization of Inlet Channel and Basin

The CFD simulations revealed a well-defined, nonlinear relationship between the geometric parameters of the inlet channel and the resulting vortex circulation. As presented in Table 3, the configuration consisting of four channel turns combined with a 13° inclination angle yielded the highest circulation value, reaching 1.3459 m^2/s. This configuration demonstrated a clear enhancement in vortex intensity compared to other design variations.

Table 3. Circulation results for different inlet channel configurations.

Number of Turns (N)	Inclination Angle (θ)	Circulation (Γ) (m^2/s)
2	13°	1.1918
2	15°	1.0670
2	17°	0.9500
3	13°	1.2700
3	15°	1.0890
3	17°	0.9120
4	13°	1.3459
4	15°	1.0977
4	17°	0.8492

An analysis of the results reveals that, in general, increasing the number of channel turns improved Γ, likely due to the extended flow path promoting angular momentum transfer into the vortex basin. Conversely, increasing the θ from 13° to 17° consistently led to a reduction in Γ across all values of N. This behavior can be attributed to a steeper descent reducing the lateral component of velocity, which is essential for sustaining vortex motion. Notably, the configuration with $N = 4$ and the steepest inclination ($\theta = 17°$) produced the lowest Γ (0.8492 m^2/s, confirming a detrimental effect at high angles. The best-performing design ($N = 4$, $\theta = 13°$) achieved a circulation value approximately 58.5% higher than the least effective configuration (N = 4, $\theta = 17°$).

To further analyze the influence of the geometric parameters, a quadratic regression model was fitted to the circulation data. The resulting response surface is given by Equation (9).

$$\Gamma(N, \theta) = 1.0328 + 0.5324N - 0.0104\theta - 0.0068N^2 + 0.0005\theta^2 - 0.0319(N \cdot \theta) \quad (9)$$

Statistical validation of the model confirmed its reliability, with an adjusted $R^2_{adj} = 0.9994$, indicating an excellent fit to the data. The analysis of variance (ANOVA) results for the quadratic response-surface model are presented in Table 4. The analysis of regression coefficients showed that the linear term associated with the inclination angle θ and the interaction term $N \cdot \theta$ have a highly significant effect on circulation ($p < 0.001$). This confirms that the inclination exerts a dominant influence on Γ, with the number of turns contributing mainly through its interaction with θ.

The quadratic regression model expressed in Equation (9) represents a local empirical approximation of the system response derived from a bounded experimental domain based on treatments obtained through numerical simulation and, as such, is subject to inherent limitations. Its validity is restricted to the specific ranges of channel turns and inclination angles explored in the computational design of experiments, and its predictive reliability cannot be guaranteed outside this parametric space. The quadratic form captures first-order interactions and moderate curvature of the response surface, but it cannot represent higher-order nonlinearities, potential flow-regime transitions, or complex hydrodynamic phenomena such as vortex breakdown, turbulence–geometry coupling, or scale-dependent effects.

In addition, the regression coefficients implicitly embed the influence of CFD modeling assumptions, mesh resolution, idealized boundary conditions, and the omission of certain loss mechanisms (e.g., surface roughness, runner shaft, and mechanical losses), which may distort extrapolated predictions. For configurations involving significantly different Reynolds numbers, geometric scales, or inlet–runner coupling conditions, both the magnitude and functional structure of the interaction terms in Equation (9) may change, leading to altered vortex dynamics and inlet-flow characteristics. Consequently, Equation (9) should be interpreted as a domain-specific phenomenological model suitable for interpolation within the ranges explored via numerical simulation, rather than as a generalizable physical law, and its extension to untested configurations requires additional simulations or re-calibration to preserve physical consistency and predictive accuracy.

The relationship between Γ and η is complex and non-linear. While circulation is indicative of swirl intensity and angular momentum in the vortex core, high circulation does not automatically translate into high efficiency. Efficiency depends on how effectively the angular momentum is transferred to the runner, which is influenced by inflow angle alignment, velocity gradients, turbulence intensity, and viscous or mixing losses. In the present design, the Nazca-inspired inlet produces relatively high circulation, but distributed inflow, wall–fluid interactions, and altered velocity profiles reduce the effective torque delivered to the runner. This decoupling highlights a key limitation of using circulation alone as an optimization criterion: it represents the strength and coherence of the vortex but cannot capture losses associated with flow misalignment or local dissipation. Consequently, turbine efficiency must be evaluated considering both circulation and additional hydraulic factors, emphasizing the need for multi-objective design approaches that integrate vortex characteristics, inflow structure, and energy dissipation mechanisms.

To ensure the validity of the regression model, a residual analysis was carried out. Table 5 summarizes the statistical tests performed to check for normality, independence, and homoscedasticity.

Table 4. ANOVA for the quadratic response-surface model.

Term	Degrees of Freedom (df)	Sum of Squares (SS)	Mean Sum of Squares (MS)	F-Ratio	*p*-Value
N	1	0.00117	0.00117	74.27	0.0033
θ	1	0.20039	0.20039	12,685.07	1.54×10^{-6}
N^2	1	0.00009	0.00009	5.77	0.0957
θ^2	1	0.00001	0.00001	0.48	0.5377
$N \cdot \theta$	1	0.01624	0.01624	1028.27	6.66×10^{-5}
Residual	3	0.00005	0.00002		–

Table 5. Statistical tests for model validation.

Test	*p*-Value
Shapiro–Wilk (normality)	0.957
Cramer–von Mises (normality)	0.913
Anderson–Darling (normality)	0.939
Durbin–Watson (independence)	0.081
Breusch–Pagan (homoscedasticity)	0.248

The Q–Q plot in Figure 14 visually confirms that the residuals closely follow a normal distribution, supporting the results of the normality tests.

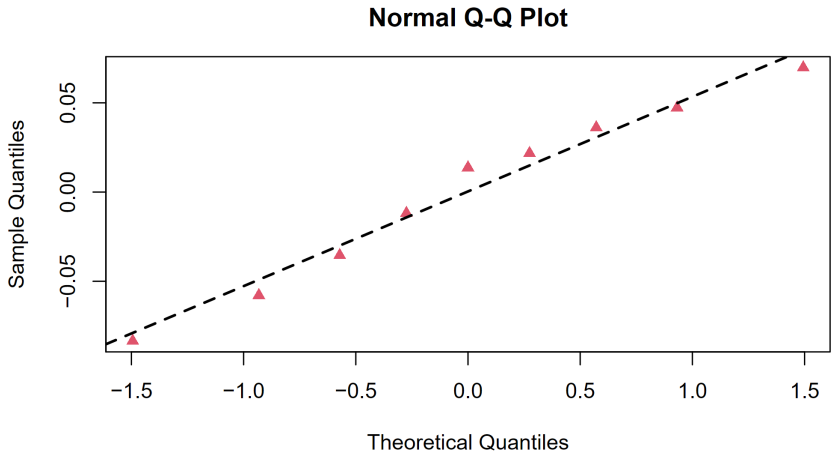


Figure 14. Q–Q plot of residuals, confirming normality.

The Durbin-Watson test yielded a *p*-value of 0.081, indicating no significant autocorrelation in the residuals. Additionally, the Breusch-Pagan test showed a *p*-value of 0.248, suggesting that the assumption of homoscedasticity is valid, as no significant heteroscedasticity was detected.

These results confirm that the quadratic regression model meets the essential statistical assumptions and is suitable for predicting circulation values based on the studied geometric parameters.

Figure 15 presents the response surface for Γ as a function of N and θ. The fitted surface predicted a maximum circulation of $\Gamma \approx 1.3447\ \mathrm{m}^2$ at $N = 4, \theta = 13^\circ$, in excellent agreement with the highest simulated value ($1.3459\ \mathrm{m}^2/\mathrm{s}$) obtained for the same configuration.

Based on these results, the configuration with $N = 4$ and $\theta = 13^\circ$ was selected as the optimal geometry for the inlet channel and basin, and was subsequently adopted for the runner design and construction of the experimental prototype.

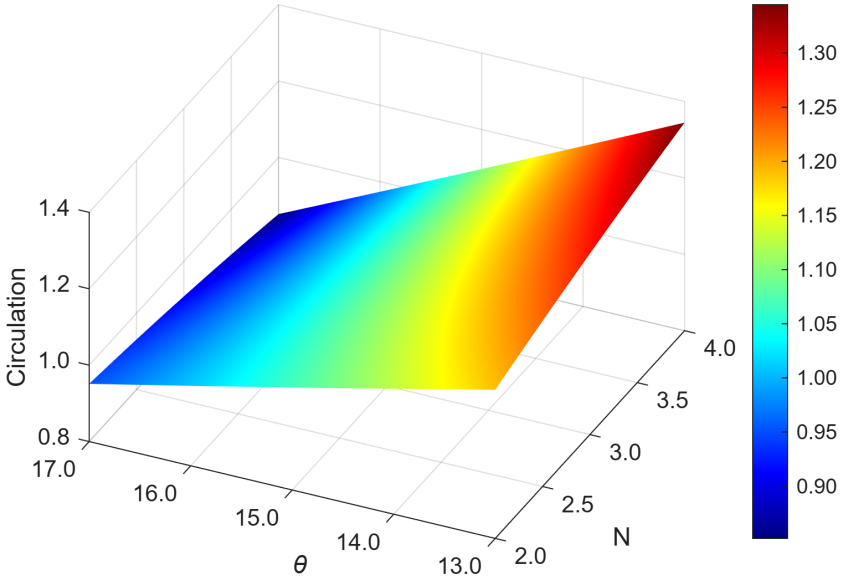


Figure 15. Response surface of circulation as a function of N and θ.

The optimized spiral inlet can be compared to the wrap-around inlet channel design proposed by Velásquez et al. [18], which served as the geometric reference for this work. In that study, the authors optimized a wrap-around channel feeding a conical basin and reported a maximum circulation of $\Gamma = 2.1074\ \mathrm{m}^2/\mathrm{s}$ for their best-performing configuration, whereas the optimal Nazca-inspired inlet developed here achieved a peak circulation of $\Gamma = 1.3459\ \mathrm{m}^2/\mathrm{s}$, which is approximately 36% lower. This difference is attributed to the fact that the spiral configuration increases the effective flow path length and wall–fluid interaction, generating higher viscous losses and reducing the net angular momentum reaching the vortex core. The distributed inflow further weakens the pressure gradient driving the rotation, producing a less concentrated vortex structure and a broader, more diffuse velocity profile. The gradual introduction of flow along the periphery limits the direct transfer of energy to the core and promotes the development of secondary flows, local recirculation vortices, and boundary layer separation, which increase kinetic energy dissipation and reduce torque generation efficiency. In contrast, wrap-around designs concentrate the inflow toward the vortex core, maintaining a more uniform velocity profile, reducing extreme velocity gradients, and minimizing localized turbulence, which allows more effective transfer of angular momentum to the runner. Additionally, the flow orientation in wrap-around designs favors better alignment with the blades, optimizing the conversion of kinetic energy into torque and reducing losses due to misalignment. The combination of these effects physically and technically explains the lower circulation observed in the spiral configuration compared to the conventional design, as well as the importance of considering the interaction between geometry, velocity profiles, and loss mechanisms when evaluating vortex turbine inlet designs.

A direct comparison under similar hydraulic loading conditions further supports the validity of the proposed inlet geometry. Velásquez et al. [18] reported circulation values of $\Gamma \approx 1.2 - 1.4\ \mathrm{m}^2/\mathrm{s}$ for their lowest flow configuration at $Q = 0.0016\ \mathrm{m}^3/\mathrm{s}$, which are comparable to the circulation obtained in the present study for the optimal spiral inlet at $Q = 0.00143\ \mathrm{m}^3/\mathrm{s}$. This agreement indicates that, under low flow laboratory conditions, the Nazca inspired channel generates a vortex strength of the same order of magnitude as a wrap around inlet with similar non dimensional proportions, thereby validating the overall intensity of the generated vortex.

Although the circulation magnitudes are similar, the internal vortex structures differ substantially between the two inlet configurations. As shown in the radial vortex profiles in

Figure 16 and the angular velocity distributions in Figure 17, the spiral inlet introduces the flow gradually along the perimeter, producing a broader and more uniformly distributed vortex, whereas the wrap around design concentrates rotation near the core, resulting in a steeper angular velocity gradient and a more localized peak. This distinction is further evidenced by the more symmetric radial profile obtained for the spiral channel compared with the strongly core centered vortex generated by the wrap around configuration.

The physical consistency of the simulated vortex is confirmed by direct comparison with the experimental measurements of Velásquez et al. [24]. The radial profiles shown in Figure 16a,b exhibit comparable air core depths in the range of 0.9 m to 1.1 m, confirming that the proposed conical discharge geometry sustains a fully developed gravitational vortex. Notably, the best performing configuration in the present study, indicated by the green squares in Figure 16a, exhibits a steeper slope along the vortex walls than the more open profiles reported by Velásquez, for example in Run 35, which indicates more effective flow confinement and improved conservation of angular momentum attributable to the spiral inlet design.

The angular velocity distributions shown in Figure 17 further confirm the dynamic consistency of the model. The peak angular velocities obtained in the present study range from approximately 70 rad/s for the optimal configuration to 90 rad/s for the inefficient configuration, as illustrated in Figure 17a, which are of the same order of magnitude as those reported by Velásquez et al. in Figure 17b, particularly their high velocity case Run 54 at approximately 80 rad/s. Unlike the broader and more diffuse peaks observed in the experimental data, the present results show more defined and centered peaks, indicating a more controlled spatial distribution of angular momentum.

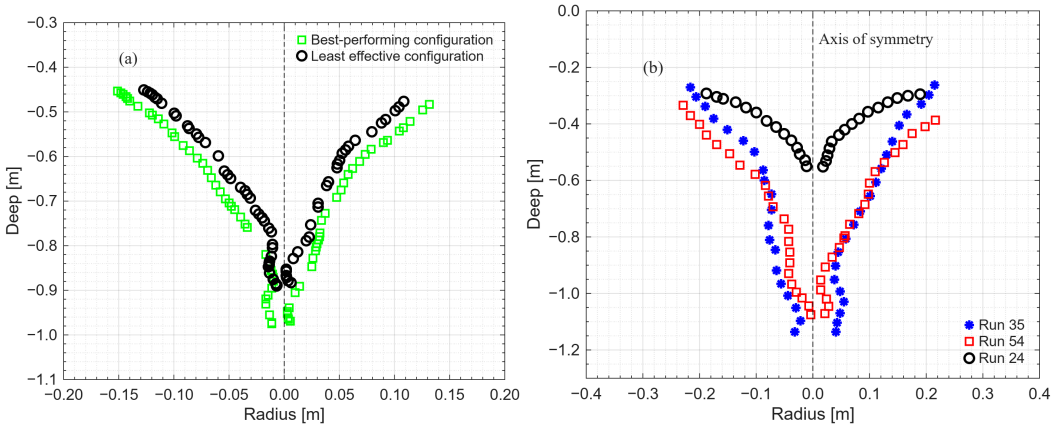


Figure 16. Radial vortex profile: (**a**) Present study and (**b**) Velásquez et al. [18].

These structural differences in vortex topology have direct implications for turbine performance. As evidenced by the more symmetric radial velocity profile in Figure 16, lateral pressure imbalances and associated radial forces on the runner shaft are reduced. At the same time, avoiding excessive concentration of angular momentum in the core, as illustrated by the wider velocity distribution in Figure 17, mitigates instability and promotes more effective blade interaction. As reported by Maika et al. [13], extremely high core angular velocities can lead to suboptimal energy extraction if part of the flow bypasses the blades. From a torque transfer perspective, a more uniform velocity field across the radius provides a more homogeneous impulse along the blade span, resulting in smoother and more stable torque delivery to the runner.

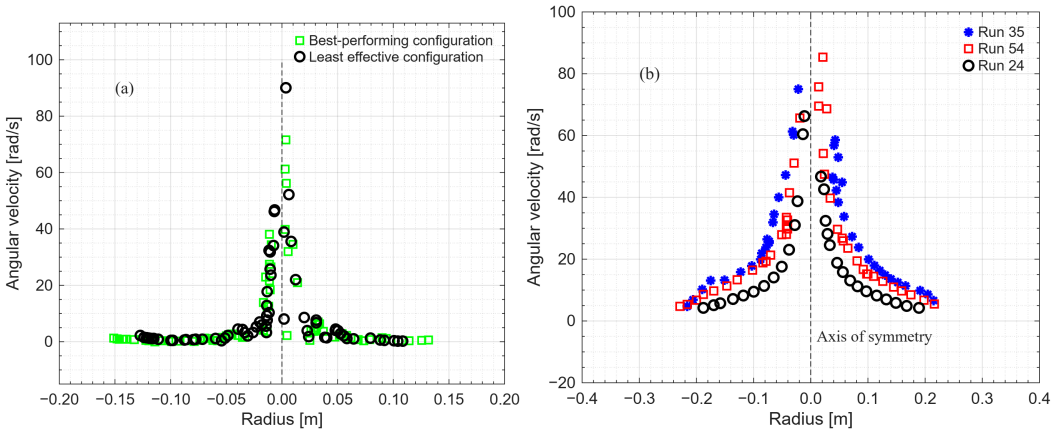


Figure 17. Angular velocity distribution: (**a**) Present study and (**b**) Velásquez et al. [18].

3.3. Hydrodynamic Performance of the Runner

Figure 18 shows the efficiency curves as a function of rotational speed for both Runner 1 and Runner 2, evaluated within the 50–150 rpm range. The results correspond to the CFD predictions obtained under identical hydraulic conditions for both geometries. Both runners exhibit nonlinear behavior, with an increase in efficiency as the rotation speed increases from 50 rpm to around 100 rpm, followed by a gradual decrease towards 150 rpm. This pattern is consistent with previous studies on gravitational vortex turbines, where an optimal operating window is typically observed in the mid-range of rotational speeds, beyond which misalignment between the vortex core and the blade path and increased turbulence reduce energy conversion efficiency [22–25].

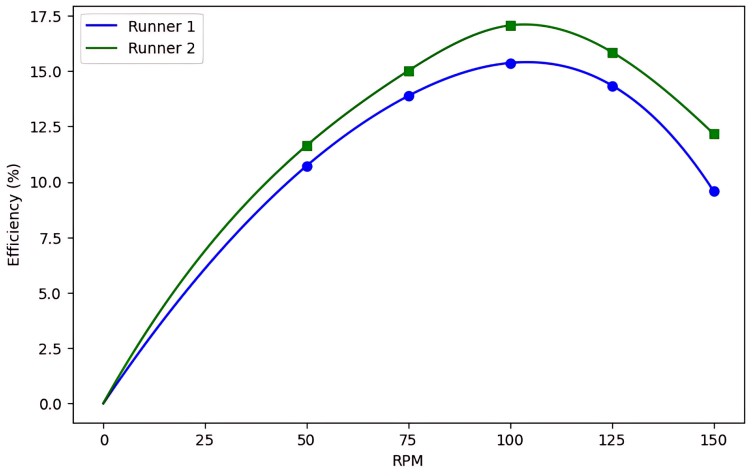
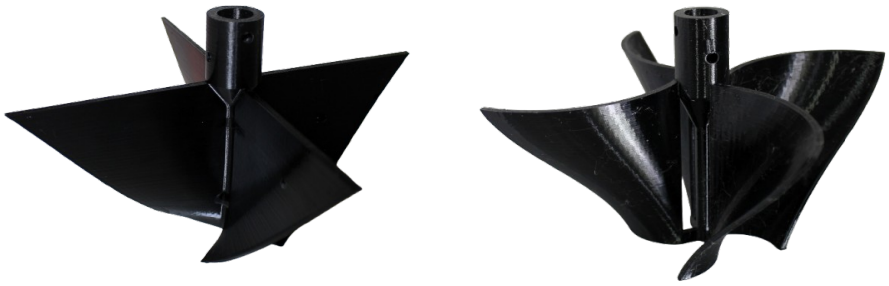


Figure 18. Efficiency curves of Runner 1 and Runner 2 as a function of rotational speed.

Runner 2, featuring curved cross-flow blades, outperformed Runner 1 at all tested speeds, reaching a peak efficiency of 17.07% at 100 rpm. Runner 1, with twisted blades, showed a lower overall performance, with a maximum efficiency of 15.37% under the same operating conditions. A quantitative comparison of the CFD results shows that the efficiency gain provided by Runner 2 ranged from approximately 0.9 to 2.6 percentage points across the investigated speeds, with an average increase of about 1.6 percentage points over Runner 1. These findings highlight the enhanced hydrodynamic interaction achieved by Runner 2, whose geometry appears better suited to the vortex dynamics generated by the optimized inlet and basin configuration.

3.4. Experimental Validation

To validate the numerical predictions, the optimized inlet channel and both runner designs were fabricated as a laboratory-scale prototype and tested under the same hydraulic conditions as the CFD simulations. Figure 19 shows the manufactured Runner 1 and Runner 2.



(a) (b)

Figure 19. 3D-printed runners used in the experimental validation: (**a**) Runner 1 and (**b**) Runner 2.

The experimental campaign consisted of sweeping the rotational speed from 0 to 150 rpm by applying discrete electrical braking loads and recording the resulting torque at each steady state point. The prototype operating under steady vortex conditions is shown in Figure 20.

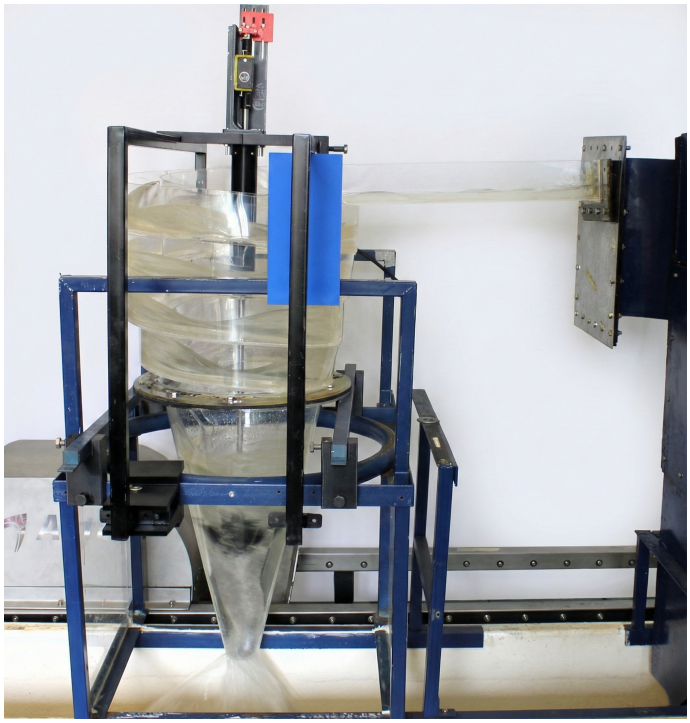
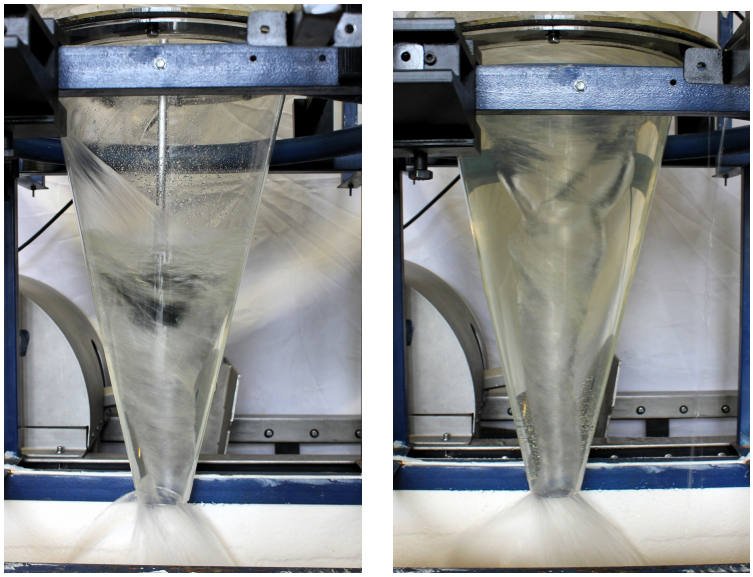


Figure 20. Laboratory-scale gravitational vortex turbine prototype in operation.

Visual inspection of the flow showed that, without the runner installed, the spiral-inlet configuration generated a coherent helical vortex with a well-defined free surface. Adding the runner changed the vortex: it became shorter and its base widened, but it stayed centered and stable, indicating that the optimized channel still induced a usable swirling flow under load. These features are illustrated in Figure 21, which compares the vortex with and without the runner.



(a) (b)

Figure 21. Vortex observed in the basin during the experiments, (**a**) with and (**b**) without the runner.

Compared with previous experimental and numerical studies conducted in conical basins, our results for a conical basin with a spiral inlet show substantially lower efficiencies. Bajracharya et al. reported a maximum efficiency of 47.8% using a conical chamber with a tangential inlet and a runner positioned at 65% of the basin height [26]. Sharif et al. achieved a maximum efficiency of 54.44% in a conical basin with a rectangular inlet channel [27]. In a later study, Sharif et al. incorporated a baffle in the tangential inlet and obtained a maximum efficiency of 43% with a five blade runner [28]. Ullah et al., using a conical basin with a spiral inlet and a four blade Savonius runner, identified the optimal runner position at 60% of the basin height, although no specific peak efficiency value was reported [29]. Muhammad et al. [30] studied a conical basin with a cone angle of 23° and associated the optimal operating conditions with the maximum efficiency and power output of the system. Edirisinghe et al., using a conical design with a spiral inlet, reported a maximum efficiency of 60.5% for a flow rate of 60 m^3/h and a head of 0.5 m [21]. Sinaga et al. analyzed double stage vortex turbines in a conical basin with a tangential inlet and obtained an efficiency of 28.92% [31]. Betancour et al. employed a conical basin with a tangential inlet and reported an efficiency of 49.5% [22]. Velásquez et al., in a numerical study with a conical basin and a spiral inlet, achieved a maximum efficiency of 60.77% [24]. Setiawan et al. reported a maximum efficiency of 28% in a conical basin with a tangential inlet [32]. In contrast, as shown in Figure 22, our experimental results for a conical basin with a spiral inlet indicate considerably lower absolute efficiencies.

Figure 22 compares the experimentally measured efficiency curves for Runner 1 and Runner 2 with their CFD counterparts. Both runners followed the same qualitative behavior predicted numerically: efficiency increased as the rotational speed rose from 50 to around 100 rpm, then dropped again towards 150 rpm. Runner 2 consistently outperformed Runner 1, whose maximum experimental efficiency was $\eta_{exp} = 8.70\%$ at $\omega = 110.79$ rpm (compared to the simulated value of 15.37% at 100 rpm). Runner 2 reached $\eta_{exp} = 11.61\%$ at $\omega = 109.23$ rpm, whereas the CFD model predicted 17.07% at 100 rpm. Even though the absolute efficiencies were lower, the experimental and simulated curves matched closely in shape and in the location of the peak.

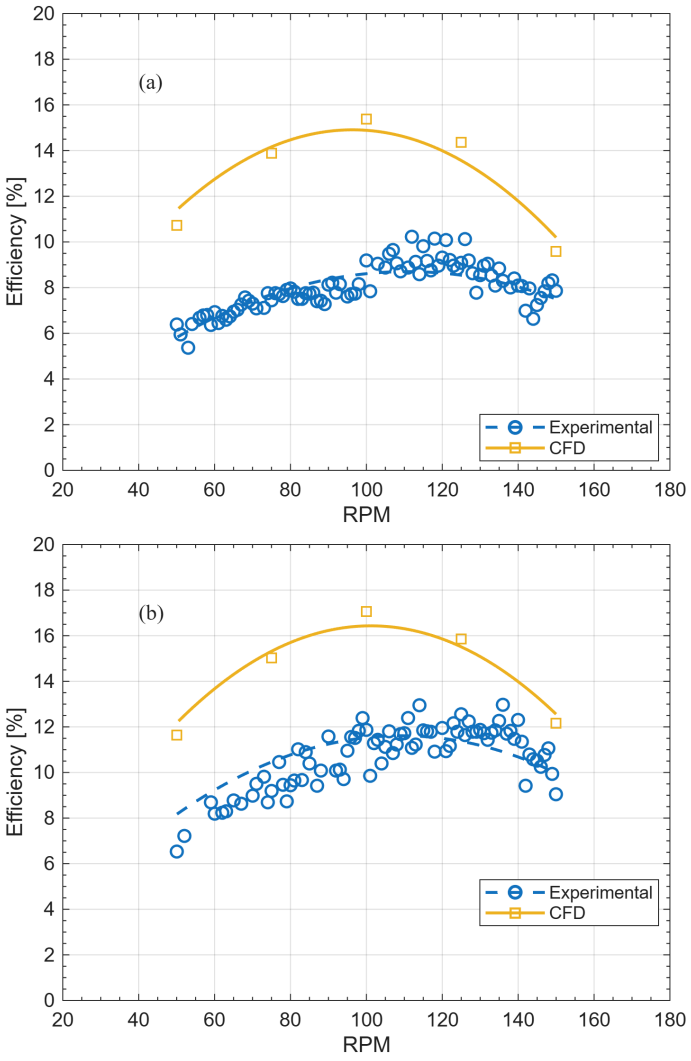


Figure 22. Comparison of experimental and simulated efficiency for (**a**) Runner 1 and (**b**) Runner 2.

The observed discrepancy between experimental results and CFD simulations, on the order of 30–40%, can be primarily attributed to geometric deviations introduced during the manual fabrication of the inlet and discharge channel, which made it difficult to maintain the dimensions and angles defined in the optimized model. The channel ended up 20–27% narrower, with the straight section approximately 5% longer, the inclination angle reduced from 13° to 4.5°, and the discharge cone opening increased by around 67%. Each of these modifications affects the flow in specific ways: the narrowing increases local fluid velocity due to continuity, but also enhances wall–fluid interaction and viscous shear, increasing frictional losses; the increased channel length extends the flow path, promoting energy dissipation and reducing angular momentum before it reaches the vortex core; the reduced inclination angle decreases the tangential velocity component delivered to the vortex, weakening rotation; and the larger discharge opening lowers the exit velocity and the pressure gradient driving the rotational flow, producing a less concentrated vortex and reducing circulation. From a physical standpoint, reducing the inclination angle modifies the balance between gravitational acceleration and tangential flow development, leading to a weaker axial component, altered residence time within the channel, and a different distribution of angular momentum at the vortex core. These changes affect the inflow structure delivered to the runner and can influence both torque generation and overall efficiency. Together, these geometric changes intensify velocity gradients and turbulence, increase kinetic energy dissipation, and reduce the efficiency of angular momentum transfer to the runner.

This physical analysis provides a coherent explanation for the lower tangential velocity and reduced efficiency observed in the prototype, demonstrating how small dimensional variations, particularly in a manual fabrication process, can amplify hydraulic losses and generate the discrepancy between CFD and experimental results. Second, the CFD model assumes ideal conditions, including smooth walls, perfectly aligned components, and the absence of mechanical losses, which leads to an overestimation of vortex stability and energy transfer. In reality, friction in the bearings, slight shaft misalignment, vibrations, and the surface roughness of the FDM-printed runners contribute to energy dissipation that is not captured in the simulations. The absence of the runner shaft in the CFD model further limits the representation of the physical system: in the experiment, the shaft obstructs part of the flow, alters local velocity profiles, and interacts with the vortex, reducing the effective angular momentum transferred to the runner. Moreover, the shaft can induce vibrations along its length despite the use of dual bearing supports, producing additional mechanical losses and small variations in torque measurements. Surface roughness of the 3D-printed components enhances wall–fluid friction and promotes localized turbulence, increasing viscous dissipation before the flow reaches the runner. Finally, small fluctuations in flow rate, imperfections in assembly, or sealant beads at panel joints introduce further losses that decrease efficiency in practice. These combined factors provide a physically consistent explanation for the systematic overprediction of efficiency by the CFD model relative to the experimental measurements.

The constrained hydraulic efficiency observed in the simulation and esperimental results are primarily attributed to the mismatch between the blade leading-edge angle of attack and the velocity vector of the incoming flow. The streamline analysis (particularly for runner 1, Figure 10) reveals regions of flow separation and recirculating vortices within the inter-blade passages, which constitute physical evidence of an inadequate incidence angle that prevents the fluid from following the blade profile curvature. This angular incongruence causes a significant fraction of the available energy not to be transferred as lift, but instead to be dissipated in the form of turbulence, resulting in elevated outlet velocities (up to 5.07 m/s). Consequently, the runner redesign strategy for performance optimization should be based on adjusting the blade twist angles to match the local flow angles along the radial direction, thereby ensuring a smooth tangential entry, minimizing boundary-layer separation, and maximizing angular momentum conversion.

In GVT, the risk of cavitation is low due to the typical operating conditions, characterized by low head and free-surface flow. From a physical standpoint, cavitation occurs when the local static pressure drops below the vapor pressure of water, leading to the formation of vapor bubbles that can collapse, causing blade erosion, vibrations, and efficiency losses. In this type of turbine, the vortex core may experience a pressure depression induced by centrifugal effects; however, since the system is open to the atmosphere and operates at relatively low rotational speeds, the minimum pressures in the core rarely approach vapor pressure. Furthermore, the open geometry and low hydraulic load favor a continuous, unconstrained flow, reducing the likelihood of localized cavitation. The risk could increase under conditions of significantly higher heads, elevated rotational speeds, or runner blades with pronounced curvatures that generate strong local accelerations, potentially affecting flow stability, torque transfer, and runner integrity. Under the operating conditions considered in this study, cavitation is not expected to pose a critical risk for the prototype. Nevertheless, future designs operating at higher loads should include pressure measurements or CFD simulations incorporating vapor pressure to explicitly assess cavitation margins.

4. Conclusions

This study examined the hydraulic and energetic performance of a GVT whose inlet channel geometry was inspired by the spiral *ojos de agua* of the Nazca culture. A combined methodology of geometric parametrization, CFD simulations, RSM, and laboratory-scale experiments was used to evaluate how this ancestral spiral concept affects vortex formation and energy conversion.

The full factorial design (3^2) applied to the Nazca-inspired inlet showed that vortex circulation (Γ) is highly sensitive to the inclination angle (θ) of the spiral channel. The CFD simulations, analyzed using a quadratic response-surface model with excellent statistical performance (adjusted $R^2_{adj} \approx 0.999$), identified the configuration with $N = 4$ and $\theta = 13^\circ$ as the optimal one. This setup produced a circulation of $\Gamma = 1.3459$ m^2/s, which is about 58% higher than the least effective configuration within the tested range. Compared with the wrap-around inlet optimized by Velásquez et al. [18], the Nazca-inspired spiral has lower maximum circulation than their best-performing design, but under similar low-flow conditions ($Q \approx 0.00143$ m^3/s versus 0.0016 m^3/s both inlets generate circulation values of comparable magnitude. In addition, the spiral channel produces a broader and more symmetrical radial vortex profile and a smoother angular velocity distribution than the wrap-around configuration, which tends to concentrate rotation near the core. These features are favorable from a torque-transfer point of view, as they reduce radial load asymmetries on the runner and promote a more homogeneous momentum exchange along the blade span [13,24].

Two runner geometries were evaluated in combination with the optimized spiral inlet: (i) Runner 1, with twisted blades, and (ii) Runner 2, featuring curved cross-flow blades. The CFD simulations predicted nonlinear efficiency curves, each peaking around 100 rpm and indicated that Runner 2 consistently outperforms Runner 1, with a simulated maximum efficiency of 17.07%, while Runner 1 reached 15.37%. These results confirm that, once the inlet geometry has been optimized, runner design remains a critical factor in improving the overall turbine performance.

Experimental tests conducted on a laboratory-scale prototype, operating at $Q = 1.4$ L/s, validated the numerical trends. The Nazca-inspired channel generated a coherent and stable vortex with and without the runner installed. Measured efficiency curves for both runners reproduced the qualitative behavior predicted by CFD, including the location of the optimum near 100 rpm and the superior performance of Runner 2. Quantitatively, the maximum experimental efficiencies were $\eta_{\text{exp}} = 8.70\%$ for Runner 1 and $\eta_{\text{exp}} = 11.61\%$ for Runner 2, about 30–40% lower than the corresponding simulated values. This discrepancy is consistent with the geometric deviations identified between the digital model and the physical prototype (the channel turned out to be slightly narrower, the inclination angle was smaller, and the discharge opening was larger), as well as with additional losses due to wall roughness, assembly imperfections and mechanical friction, none of which are included in the CFD model.

From a broader perspective, these results show that a Nazca-inspired spiral inlet can create a stable and hydraulically effective vortex, that matches the circulation levels observed in a wrap-around channel under low-flow and low-head conditions. However, in terms of absolute efficiency, the present configuration does not outperform conventional reported GVT designs. This highlights that morphological inspiration from ancient hydraulic works, while valuable as a source of geometric concepts, must be complemented by rigorous hydrodynamic optimization, careful consideration of manufacturability, and integrated runner–channel co-design in order to translate geometric novelty into clear performance gains.

Future work should focus on narrowing the gap between numerical predictions and prototype behavior by addressing all the limitations identified in the present study. In particular, geometric mismatches introduced during manual fabrication, including variations in channel width, length, inclination angle, and discharge opening, should be minimized. The use of advanced additive manufacturing techniques capable of producing continuous helical surfaces, rather than segmented assemblies, could reduce alignment errors and fabrication discontinuities, improving vortex formation and hydraulic efficiency. Integrated runner–channel modifications are also recommended, including: (i) reshaping the spiral channel cross section to a gradually contracting or cambered profile to better conserve tangential momentum and limit wall-induced viscous losses; (ii) introducing a short transition or guide section near the channel outlet to redirect peripheral flow more directly toward the vortex core, increasing angular momentum concentration before interaction with the runner; and (iii) redesigning the runner blades with variable inlet angles and camber tailored to the non-uniform inflow generated by the spiral channel, reducing incidence losses and improving torque extraction. Furthermore, including effects such as surface roughness of the 3D-printed runners, the presence of the runner shaft, and mechanical losses in CFD simulations would allow a more realistic representation of experimental behavior. Finally, extending the parametric study to a wider range of heads and flow rates, as well as considering additional geometric and operational variables (basin height, discharge opening shapes, and new combinations of factors), would provide a more robust and generalizable design framework for bio-inspired gravitational vortex turbines.

Author Contributions: Conceptualization, J.C.G., A.R.-C. and E.C.; Methodology, J.C.G., A.R.-C. and E.C.; Software, J.C.G.; Validation, J.C.G.; Formal analysis, J.C.G., A.R.-C. and E.C.; Writing—original draft, J.C.G., A.R.-C. and E.C.; Writing— review & editing, A.R.-C. and E.C.; Supervision, E.C.; Project administration, A.R.-C. and E.C.; Funding acquisition, E.C. All authors have read and agreed to the published version of the manuscript.

Funding: We acknowledge the financial support provided by the announcement no. 890 de 2020 Convocatoria para el fortalecimiento de CTeI en Instituciones de Educación Superior (IES) Públicas 2020 (contract no. 2022-0453).

Data Availability Statement: The original contributions presented in the study are included in the article, further inquiries can be directed to the corresponding author.

Conflicts of Interest: The authors declare that they have no conflict of interest that could potentially influence the findings presented in this work.

References

1. IEA. Global Energy Crisis. 2023. Available online: https://www.iea.org/topics/global-energy-crisis (accessed on 30 July 2024).
2. Soeder, D.J. Fossil Fuels and Climate Change. In *Fracking and the Environment: A Scientific Assessment of the Environmental Risks from Hydraulic Fracturing and Fossil Fuels*; Springer International Publishing: Cham, Switzerland, 2021; pp. 155–185. [CrossRef]
3. Kweku, D.W.; Bismark, O.; Maxwell, A.; Desmond, K.A.; Danso, K.B.; Oti-Mensah, E.A.; Quachie, A.T.; Adormaa, B.B. Greenhouse Effect: Greenhouse Gases and Their Impact on Global Warming. *J. Sci. Res. Rep.* **2018**, *17*, 1–9. [CrossRef]
4. ClientEarth. Fossil Fuels and Climate Change: The Facts. Available online: https://www.clientearth.org/latest/news/fossil-fuels-and-climate-change-the-facts/ (accessed on 30 July 2024).
5. Owusu, P.A.; Asumadu-Sarkodie, S. A review of renewable energy sources, sustainability issues and climate change mitigation. *Cogent Eng.* **2016**, *3*, 1167990. [CrossRef]
6. Kabeyi, M.J.B.; Olanrewaju, O.A. Sustainable Energy Transition for Renewable and Low Carbon Grid Electricity Generation and Supply. *Front. Energy Res.* **2022**, *9*, 743114. [CrossRef]
7. Siemonsmeier, M.; Baumanns, P.; van Bracht, N.; Schönefeld, M.; Schönbauer, A.; Moser, A.; Dahlhaug, O.G.; Heidenreich, S. *Hydropower Providing Flexibility for a Renewable Energy System: Three European Energy Scenarios*; HydroFlex: Trondheim, Norway, 2018.

8. Lobus, N.V.; Knyazeva, M.A.; Popova, A.F.; Kulikovskiy, M.S. Carbon Footprint Reduction and Climate Change Mitigation: A Review of the Approaches, Technologies, and Implementation Challenges. *C* **2023**, *9*, 120. [CrossRef]
9. Silva, S.N.; Álvarez del Castillo, J. An Approach of the Hydropower: Advantages and Impacts. A Review. *J. Energy Res. Rev.* **2021**, *8*, 10–20. [CrossRef]
10. Tsuanyo, D.; Amougou, B.; Aziz, A.; Nka Nnomo, B.; Fioriti, D.; Kenfack, J. Design models for small run-of-river hydropower plants: A review. *Sustain. Energy Res.* **2023**, *10*, 3. [CrossRef]
11. Dhakal, S.; Timilsina, A.B.; Dhakal, R.; Fuyal, D.; Bajracharya, T.R.; Pandit, H.P.; Amatya, N.; Nakarmi, A.M. Comparison of cylindrical and conical basins with optimum position of runner: Gravitational water vortex power plant. *Renew. Sustain. Energy Rev.* **2015**, *48*, 662–669. [CrossRef]
12. Edirisinghe, D.S.; Yang, H.-S.; Gunawardane, S.D.G.S.P.; Lee, Y.-H. Enhancing the performance of gravitational water vortex turbine by flow simulation analysis. *Renew. Energy* **2022**, *194*, 163–180. [CrossRef]
13. Maika, N.; Lin, W.; Khatamifar, M. A Review of Gravitational Water Vortex Hydro Turbine Systems for Hydropower Generation. *Energies* **2023**, *16*, 5394. [CrossRef]
14. Saleem, A.S.; Rizwanullah; Cheema, T.A. Experimental Investigation of Various Blade Configurations of Gravitational Water Vortex Turbine (GWVT). In Proceedings of the 2018 International Conference on Power Generation Systems and Renewable Energy Technologies (PGSRET), Islamabad, Pakistan, 10–12 September 2018; pp. 1–5. [CrossRef]
15. Esenarro, D.; Vilchez, J.; Adrianzen, M.; Raymundo, V.; Gómez, A.; Cobeñas, P. Management Techniques of Ancestral Hydraulic Systems, Nasca, Peru; Marrakech, Morocco; and Tabriz, Iran in Different Civilizations with Arid Climates. *Water* **2023**, *15*, 3407. [CrossRef]
16. Lasaponara, R.; Lancho Rojas, J.; Masini, N. Puquios: The Nasca Response to Water Shortage. In *The Ancient Nasca World: New Insights from Science and Archaeology*; Lasaponara, R., Masini, N., Orefici, G., Eds.; Springer International Publishing: Cham, Switzerland, 2016; pp. 279–327. [CrossRef]
17. Myers, R.H.; Montgomery, D.C.; Anderson-Cook, C.M. *Response Surface Methodology: Process and Product Optimization Using Designed Experiments*; John Wiley & Sons: Hoboken, NJ, USA, 2016; ISBN 978-1-118-91601-8.
18. Velásquez, L.; Posada, A.; Chica, E. Surrogate modeling method for multi-objective optimization of the inlet channel and the basin of a gravitational water vortex hydraulic turbine. *Appl. Energy* **2023**, *330*, 120357. [CrossRef]
19. Faraji, A.; Jande, Y.A.C.; Kivevele, T. Performance analysis of a runner for gravitational water vortex power plant. *Energy Sci. Eng.* **2022**, *10*, 1055–1066. [CrossRef]
20. Velásquez, L.; Posada, A.; Chica, E. Optimization of the basin and inlet channel of a gravitational water vortex hydraulic turbine using the response surface methodology. *Renew. Energy* **2022**, *187*, 508–521. [CrossRef]
21. Edirisinghe, D.S.; Yang, H.S.; Gunawardane, S.D.G.S.P.; Alkhabbaz, A.; Tongphong, W.; Yoon, M.; Lee, Y.H. Numerical and experimental investigation on water vortex power plant to recover the energy from industrial wastewater. *Renew. Energy* **2023**, *204*, 617–634. [CrossRef]
22. Betancour, J.; Romero-Menco, F.; Velásquez, L.; Rubio-Clemente, A.; Chica, E. Design and optimization of a runner for a gravitational vortex turbine using the response surface methodology and experimental tests. *Renew. Energy* **2023**, *210*, 306–320. [CrossRef]
23. Khan, N.H. Blade Optimization of Gravitational Water Vortex Turbine. Master's Thesis, Ghulam Ishaq Khan Institute of Engineering Sciences and Technology, Topi, Pakistan, May 2016.
24. Velásquez, L.; Romero-Menco, F.; Rubio-Clemente, A.; Posada, A.; Chica, E. Numerical optimization and experimental validation of the runner of a gravitational water vortex hydraulic turbine with a spiral inlet channel and a conical basin. *Renew. Energy* **2024**, *220*, 119676. [CrossRef]
25. Acharya, S.; Ghimire, S.K.; Dura, H.B. Design Study of Runner for Gravitational Water Vortex Power Plant with Conical Basin. *Proc. IOE Grad. Conf.* **2019**, *6*, 100–108.
26. Bajracharya, T.R.; Shakya, S.R.; Timilsina, A.B.; Dhakal, J.; Neupane, S.; Gautam, A.; Sapkota, A. Effects of geometrical parameters in gravitational water vortex turbines with conical basin. *J. Renew. Energy* **2020**, *2020*, 5373784. [CrossRef]
27. Sharif, A.; Siddiqi, M.U.R.; Tahir, M.; Ullah, U.; Aslam, A.; Tipu, A.K.; Arif, M.; Sheikh, N.A. Investigating the effect of inlet head and water pressure on the performance of single stage gravitational water vortex turbine. *J. Mech. Eng. Res. Dev.* **2021**, *44*, 156–168.
28. Sharif, A.; Tipu, J.A.K.; Arif, M.; Abbasi, M.S.; Jabbar, A.U.; Noon, A.A.; Siddiqi, M.U.R. Performance Evaluation of a Multi-Stage Gravitational Water Vortex Turbine with optimum number of Blades. *J. Mech. Eng. Res. Dev.* **2022**, *45*, 35–43.
29. Ullah, R.; Cheema, T.A. Experimental investigation of runner design parameters on the performance of vortex turbine. *Eng. Proc.* **2022**, *23*, 14.
30. Muhammad, R.; Sharif, A.; Siddiqi, M. Performance investigation of a single-stage gravitational water vortex turbine accounting for water vortex configuration and rotational speed. *J. Eng. Appl. Sci.* **2022**, *41*, 44–55. [CrossRef]

31. Sinaga, D.A.; Septiyanto, M.D.; Arifin, Z.; Rusdiyanto, G.; Prasetyo, S.D.; Hadi, S. The Effect of Blade Distances on the Performance of Double-Stage Gravitational Water Vortex Turbine. *J. Adv. Res. Fluid Mech. Therm. Sci.* **2023**, *109*, 196–209. [CrossRef]
32. Haryadi; Sugianto; Setiawa, D. Experimental and Numerical Study on Conical Gravitational Water Vortex Turbine with 3D Runner. *J. Adv. Res. Fluid Mech. Therm. Sci.* **2024**, *114*, 1–14. [CrossRef]

Disclaimer/Publisher's Note: The statements, opinions and data contained in all publications are solely those of the individual author(s) and contributor(s) and not of MDPI and/or the editor(s). MDPI and/or the editor(s) disclaim responsibility for any injury to people or property resulting from any ideas, methods, instructions or products referred to in the content.